

Structural parameters for the Galactic dwarf spheroidals

M. Irwin¹ and D. Hatzidimitriou²

¹*Royal Greenwich Observatory, Madingley Road, Cambridge CB3 0EZ*

²*Physics Department, University of Crete, GR714-09, Heraklion, Crete, Greece*

Accepted 1995 July 13. Received 1995 June 30; in original form 1995 February 21

ABSTRACT

A new determination of the structural parameters of the dwarf spheroidals (dSphs) orbiting our Galaxy is presented. The morphology of the dSphs was determined from star counts made using photographic plates digitized and analysed using the APM facility at Cambridge. Global and central mass-to-light ratios were calculated for these galaxies. They range from ≈ 10 for Fornax and Sculptor to more than 200 for Draco. It appears plausible that Draco, Ursa Minor, Carina and Sextans contain significant amounts of dark matter, at least under the standard assumptions for the dynamics of these galaxies. However, the errors associated with these estimates remain – often forbiddingly – large, dominated (in most cases) by the errors in the luminosity and velocity dispersion. The possibility of the presence of extra-tidal stars in at least some of the dSphs is also discussed, together with the effect of the Galactic tidal field on the dSphs' morphology. Both Sextans and Sculptor appear to be good candidates for systems in the process of tidal disruption.

Key words: Galaxy: structure – galaxies: structure – dark matter.

1 INTRODUCTION

The eight¹ dwarf spheroidal galaxies (dSphs) orbiting our Galaxy are not only interesting objects per se comprising the low mass/luminosity tail of the galaxy distribution, but also provide us with important clues about the total mass and dynamics of our own Galaxy. There has recently been a significant revival of interest in the structural properties of the dSphs because of their importance in the study of the local abundance of so-called dark matter. Taken at face value, the current best estimates of the velocity dispersions of the Galactic dSphs, coupled with measures of their morphological properties, imply a large range in mass-to-light ratios for these systems. For example: at the bright end of the dSph range, Fornax seems to have $M/L \sim 5$; whilst the lowest luminosity systems Ursa Minor and Draco have $M/L \sim 100$ (e.g. Pryor 1992). This 'trend' follows the predictions of Dekel & Silk (1986) based on the assumption that dark-matter haloes exist in all galaxies. However, if the dSphs do contain copious amounts of dark matter, not only would the dark matter severely influence the formation and evolution of these systems, but the dark matter could, almost certainly, not be 'hot', e.g. in the form of massive neutrinos, if it can be confined on scales of ~ 1 kpc (Tremaine & Gunn 1979).

¹A ninth dwarf spheroidal orbiting the Galaxy was discovered in 1994 by Ibata, Gilmore & Irwin (1994).

Unfortunately, our attempts at understanding the origin and evolution of the dSphs are severely impaired by the large uncertainties in the observed structural parameters for these objects. The advent of red-sensitive large-area CCD detectors and multi-object spectrographs capable of measuring velocities accurate to a few km s^{-1} for stars on the giant branch of the Galactic dSphs, has highlighted the need for more reliable measures of these structural properties. Indeed, with multiple epoch observations of giant branch stars now available for several dSph systems (see Table 9 below), the main cause of uncertainty in producing viable models of dSphs lies in our incomplete knowledge of their structural properties (see for example, Pryor & Kormendy 1990).

Most of the previous work on the morphology of the Galactic dSphs was based on eyeball counts from photographic plates; the seminal studies of Hodge (1961a,b, 1962, 1963, 1964a,b) are particularly good examples of this work. Two notable exceptions to this were the study by Eskridge (1988a,b,c,d) of the Fornax and Sculptor systems, and the discovery and morphological analysis by Irwin et al. (1990) of the Sextans dSph – both based on automatic machine-made measurements. Over the last few years, in an attempt to improve this situation, we have been steadily accumulating data on the Galactic dSphs. Photographic plates for all eight Galactic dSphs using both the Palomar and UK Schmidt telescopes have now been measured and analysed using the

APM facility in Cambridge (Kibblewhite et al. 1984). Since the Galactic dSphs typically subtend angles ranging from one to several degrees on the sky, wide-field photographic plates taken on Schmidt telescopes are still the only viable means of estimating their global structural parameters. With the exception of Leo I, Leo II and Fornax, all the plate material goes deep enough to sample adequately the stellar population to below the level of the horizontal branch, and covers a sufficiently large area of sky ($\sim 30 \text{ deg}^2$) to give reliable estimates of the background number density. In this paper we present a new determination of the structural parameters for all eight Galactic dSphs based on the APM measurements of the Schmidt photographic plates.

The main advantages of this study are:

- (a) the methodology and type of observational data are the same for all galaxies analysed;
- (b) the 'star counting' is objective and consequently produces repeatable results when multiple plates of the same object are analysed;
- (c) an accurate estimation of the background density of objects, which is vital in interpreting the presence or otherwise of tidal cut-offs, is straightforward, and
- (d) the reality, or otherwise, of irregularities in the star distribution within each dSph can be mapped and quantified.

In Section 2, the observational material and the star-counting method are described; isopleths and density profiles for the eight dSphs are presented. In Section 3, the core and tidal radii are estimated for each system, by fitting single-component King models to the density profiles. In Section 4, the central surface brightness and the total magnitudes of the galaxies are derived. In Section 5, the two-dimensional distribution of stars is briefly described, while in Section 6 our results are compared with those of previous studies. Finally, in Section 7 the mass-to-light ratios are calculated and the possible dark-matter content of these galaxies discussed; their perigalactic distances are estimated, and the tidal effects on their structure quantitatively discussed.

2 DATA DESCRIPTION

2.1 Photographic plate material and APM measurements

All of the plates used in this study were taken with either the Palomar or the UK Schmidt telescopes. They are listed in Table 1 along with information about the emulsion and filters used, and the exposure times. Each plate covers an area of some 36 deg^2 on the sky, of which $\sim 30 \text{ deg}^2$ are directly usable, the exact area depending on the location, extent and number of calibration density wedges superposed on the plates. The plate scale for all plates is $67.15 \text{ arcsec mm}^{-1}$. All plates were digitized at a pixel sampling interval of $\sim 0.5 \text{ arcsec}$, with an effective resolution of 1 arcsec arising from the size of the sampling beam. Since the seeing-limited resolution of the plates is generally in the range $2\text{--}3 \text{ arcsec}$, this gives well-sampled data for further analysis. Images are located and parametrized automatically, such that the final output consists of a list of all images detected on the plate and a series of parameters describing their location, intensity and shape (see Irwin & Trimble 1984 and Kibblewhite et al. 1984 for further details). The image-parameter lists for all

Table 1. Plate material.

Galaxy	Plate	Plate centre (B1950)	Emulsion+filter	Exposure (min)	Telescope
Carina	J8295	$06^h45^m - 51.0^\circ$	IIIaJ + GG395	60	UKST
	OR8996	$06^h45^m - 51.5^\circ$	IIIaF + OG590	60	UKST
Draco	PS29671	$17^h12^m + 58.0^\circ$	IIIaJ + Wr4	150	Palomar
	PS29667	$17^h12^m + 58.0^\circ$	IIIaF + Wr25	75	Palomar
Fornax	J8297	$02^h38^m - 34.7^\circ$	IIIaJ + GG395	60	UKST
Leo I	O74	$10^h05^m + 11.5^\circ$	103aO	12	Palomar
	E74	$10^h05^m + 11.5^\circ$	103aE + Wr25	45	Palomar
Leo II	O1353	$11^h21^m + 23.5^\circ$	103aO	12	Palomar
	E1353	$11^h21^m + 23.5^\circ$	103aE + Wr25	50	Palomar
Sculptor	J8046c	$00^h48^m - 35.0^\circ$	IIIaJ + GG395	60	UKST
Sextans	J12465c	$10^h20^m + 00.0^\circ$	IIIaJ + GG395	120	UKST
	OR11589	$10^h20^m + 00.0^\circ$	IIIaF + OG590	120	UKST
Ursa Minor	PS29610	$15^h11^m + 67.8^\circ$	IIIaJ + Wr4	150	Palomar
	PS29666	$15^h11^m + 67.8^\circ$	IIIaF + Wr25	75	Palomar

Notes to table.

- (1) All plates cover $6 \times 6 \text{ deg}^2$ of sky at a plate scale of $67.15 \text{ arcsec mm}^{-1}$.
- (2) Plates with subscript c are glass copy UKST sky-survey plates, other UKST plates are originals.
- (3) The O and E plates are glass copies of the 1950's Palomar sky-survey plates, other Palomar plates are originals.

the plates that are shown in Table 1 comprise the basic raw material for all subsequent analysis. Typically some 250 000 images are detected on each plate down to a limiting magnitude of $B \sim 22$ for the 'blue' IIIaJ and 103aO plates, $R \sim 21$ for the 'red' IIIaF and $R \sim 20$ for the 103aE plates.

In general, no corrections for edge effects or plate emulsion sensitivity variations were made, since they were either unnecessary or unknown, respectively. Emulsion sensitivity variations can lead to systematic errors of $\pm 0.1 \text{ mag}$ over areas of typically several cm in size, but without full-scale CCD calibration it is impossible to map out these effects. Throughout this paper we have assumed that by 'averaging' number-density distributions over as large a region as possible when deriving structural parameters, we have also 'averaged' out the gross effects of these field errors. A cross-check on this assumption comes from analysing more than one plate for each field, since emulsion sensitivity variations should in general not correlate over different plates. In all cases where more than one plate was available, we could find no significant difference between structural parameters derived from different plates.

Systematic magnitude variations caused by optical vignetting (and preferential desensitization in the outer regions of a plate) could, in principle, be more of a problem. For full-size Palomar and UKST plates ($35.5 \times 35.5 \text{ cm}^2$), corrections for geometric vignetting become noticeable at radial distances beyond 2.5° from the plate centre, and rise rapidly beyond 3° (see UKSTU handbook 1983). Interior to 2.5° corrections in measured number density are negligible. In most cases the target dSph was located close to the centre of the plates available for this study. Carina, Draco, Fornax and Ursa Minor are all within $\sim 0.5^\circ$ of the plate centres since the

plates were explicitly taken to study these objects. The plates for Leo I and Leo II are glass copies of the Palomar sky survey plates. However, Leo I happens to be only 1° from the plate centre and although Leo II is approximately 2° off-centre, because of its small angular size there is no problem in adequately sampling the region around it. For both Sculptor and Sextans, only UKST survey plates were readily available, and in both galaxies the outer envelope at the ‘tidal’ radius reaches the region of the plate, where vignetting is not negligible. Consequently we have compared profile estimates made with and without a vignetting correction for these two dSphs. We found no significant differences. A further test, using only the ‘half’ of each dSph furthest from the plate boundaries, confirmed that vignetting is not a serious problem for the tidal regions in these cases. This is presumably due to the fact that vignetting affects both background counts and dSph counts equally (to first order both have similar luminosity functions near the plate limits). There is a small percentage change in the total dSph counts over and above background in vignettted regions, but averaged over the whole ‘tidal’ region this effect becomes negligible.

2.2 Corrections applied to the raw data

The construction of the isopleths described in Section 2.3 and the resulting radial profiles (Section 2.4) can be affected significantly by the following two factors:

- (i) background galaxies and clusters of galaxies in the line of sight of the dSphs;
- (ii) blending of images which are not resolved by the measuring machine; this causes increasing incompleteness with decreasing distance from the centres of the dSphs.

In principle, galaxies and galaxy clusters can be effectively removed before subsequent analysis, using the image parameters to distinguish between stellar images and galaxies. Unfortunately, within two magnitudes of the plate limit, where the majority of the image counts arise, this morphological discrimination becomes unreliable. The alternative approach – which was adopted here – is to simply treat all images equally and let the galaxies and contaminating foreground Galactic stars be statistically removed during the background-correction procedure described in Section 2.4. This latter method, however, is not effective in the case of a rich cluster of galaxies in the vicinity of the dSph, as happens to be the case with Sextans. For this dSph only, preselection of stellar images, based on morphological classification criteria, was performed.

The method chosen for accounting for background galaxies allows the use of the crowding correction described by Irwin & Trimble (1984). For example, the centre of Fornax has an apparent image number density of ≈ 30 images arcmin^{-2} ; after applying the crowding correction to allow for the blended images, the ‘true’ image number density was revealed to be approximately 100 images arcmin^{-2} ; whilst at the typical background image density of ~ 2 images arcmin^{-2} , the correction amounts to only 1 or 2 per cent. In the centre of dSphs like Fornax, the majority of images overlap with neighbours, making unbiased morphological classification very difficult. This would lead to systematic underestimation of the true stellar density as a function of distance from the centre of the dSph, since in regions of

higher object density there is a much higher chance of finding images overlapping others, thereby causing preferential selection of the non-stellar category and a subsequent depletion of apparent stellar counts towards the centres of the dSphs. This problem is an additional reason for not applying such a morphological classification scheme, as was also mentioned in the previous paragraph (note that in the case of Sextans, where such classification was employed, the central density was much lower).

To summarize, all the raw images detected were used to construct the two-dimensional isopleth maps apart from Sextans, where images classified only as stellar were used; crowding corrections following Irwin & Trimble (1984) were used to correct all the derived one-dimensional ‘radial’ profiles to statistically allow for the effects of image blending.

2.3 Isopleths

The global properties of the dSphs were derived by analysing isopleth maps of the detected image distribution. For each dSph a suitably sized region, typically $3 \times 3 \text{ deg}^2$, centred as closely as possible on the target was chosen and partitioned into a 128×128 grid of pixels. The numbers of images within the individual pixels then define the two-dimensional isopleth map.

Bright foreground objects in the line of sight of the dSph have little effect on the counts since the image analysis software finds and parametrizes other images located in their haloes and at the same time does not break up bright stars into several false images.

The isopleth maps for the eight galaxies are presented in Fig. 1. These can be analysed in the same way as any other two-dimensional map. In particular, standard isophotal analysis methods provide a simple way of estimating the centre of gravity, ellipticity $\epsilon (= 1 - b/a)$, and position angle of the number distribution. By using a series of ‘analysis’ isophotes, the variation of these quantities as a function of number density can be derived and an estimate of the errors in the parameters made. Table 2 lists the resulting centres of gravity, *mean* ellipticities and *mean* position angles, and the associated errors for the eight dSphs.

Within the errors, there were generally no significant variations of ellipticity, or position angle, with radius. Consequently, we derived the ‘radial’ profiles by measuring average counts in elliptical annuli centred on the dSph using the mean ellipticity and position angle derived from the isopleth maps listed in Table 2. In contrast, Eskridge (1988a,b,c,d), in his study of Fornax and Sculptor, allowed the ellipticity and position angle to vary in the inner regions and only used fixed annuli in the outermost parts where his derived ellipticity and position angle became unreliable.

Advantages of using a fixed pattern of elliptical annuli are that the derived radial profile is not as sensitive to errors in estimating the fitted ellipse parameters and that the profile is more readily interpretable in terms of simple dynamical models. We note, however, that Sculptor, Fornax and Ursa Minor all do show departures from simple global elliptical symmetry in their core regions which we discuss further in Section 5. Although these asymmetries make little difference to the derived average ‘radial’ profiles, they highlight the problems encountered in fitting simple relaxed dynamical models to real galaxies.

2.4 Number-density distribution and radial profiles

The 'radial' number-density distribution of the dSphs was examined, using the original lists of detected images and averaging the number counts within suitably oriented elliptical annuli centred on the dSphs. As noted before, this

method was considered preferable to the direct profile fitting applied by Eskridge (1988a,c) which fails in the outer, low signal-to-noise, regions. The values for the centre, ellipticity, and orientation (i.e. position angle) of the average ellipse are taken from Table 2. In Table 3, the raw counts (arcmin^{-2} , measured on the blue plates, apart from Leo I and II where

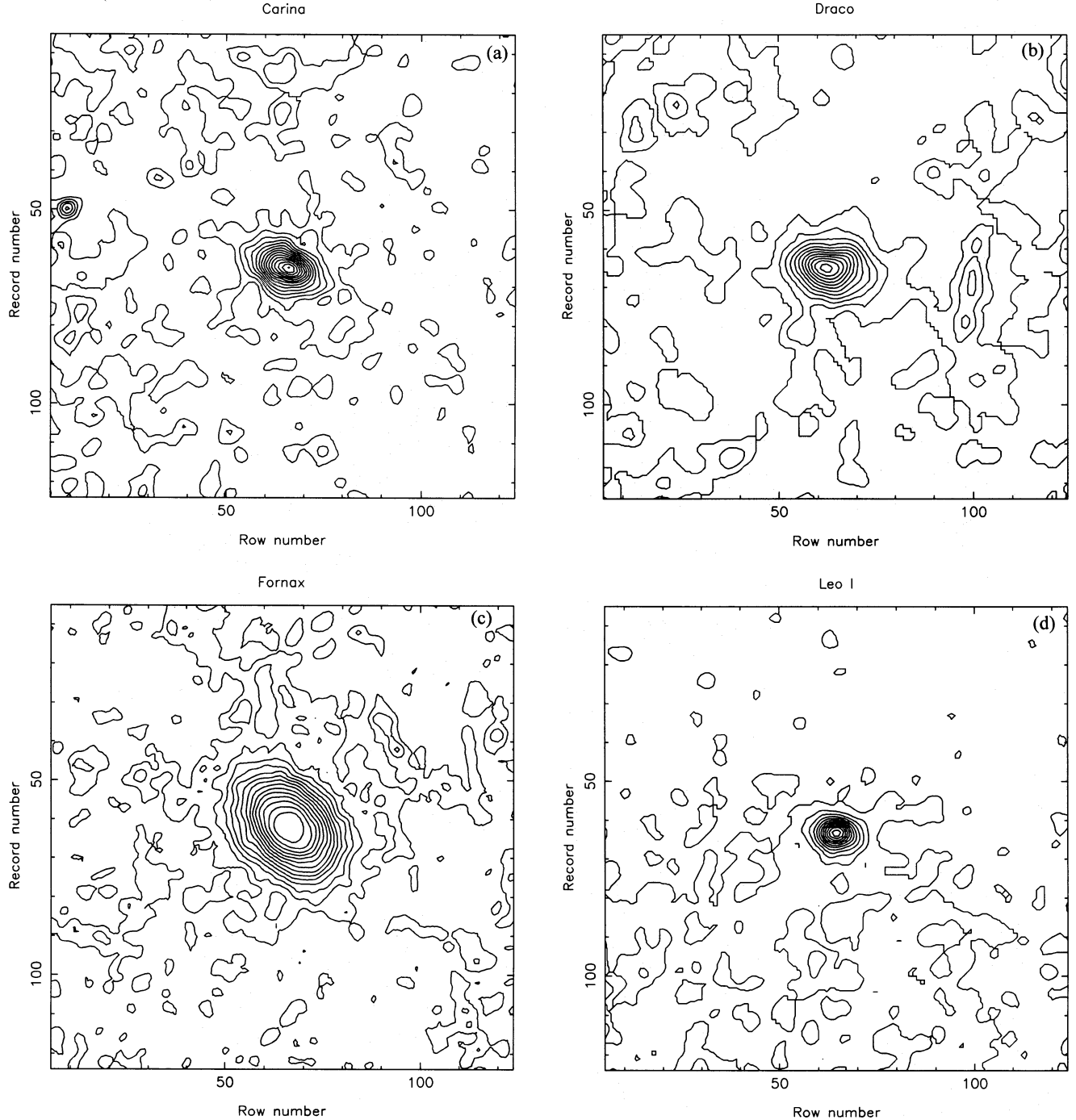


Figure 1. Isopleth maps of the eight Galactic dSphs studied. In all cases north is to the top and east to the left. The size of the regions shown and the contour levels are: (a) Carina $3.0 \times 3.0 \text{ deg}^2$; first contour 3.0 arcmin^{-2} ; contour increment 0.5 arcmin^{-2} . (b) Draco $2.3 \times 2.3 \text{ deg}^2$; first contour 2.0 arcmin^{-2} ; contour increment 0.25 arcmin^{-2} . (c) Fornax $5.1 \times 5.1 \text{ deg}^2$; first contour 1.5 arcmin^{-2} ; contour increment 0.5 arcmin^{-2} and then increasing by a factor of 1.2 per increment. (d) Leo I $2.0 \times 2.0 \text{ deg}^2$; first contour 1.3 arcmin^{-2} ; contour increment 1.0 arcmin^{-2} . (e) Leo II $1.5 \times 1.5 \text{ deg}^2$; first contour 1.7 arcmin^{-2} ; contour increment 1.0 arcmin^{-2} . (f) Sculptor $3.5 \times 3.5 \text{ deg}^2$; first contour 1.4 arcmin^{-2} ; contour increment 0.5 arcmin^{-2} and then increasing by a factor of 1.2 per increment. (g) Sextans $3.0 \times 3.0 \text{ deg}^2$; first contour 1.5 arcmin^{-2} ; contour increment 0.5 arcmin^{-2} . (h) Ursa Minor $3.4 \times 3.4 \text{ deg}^2$; first contour 1.3 arcmin^{-2} ; contour increment 0.3 arcmin^{-2} .

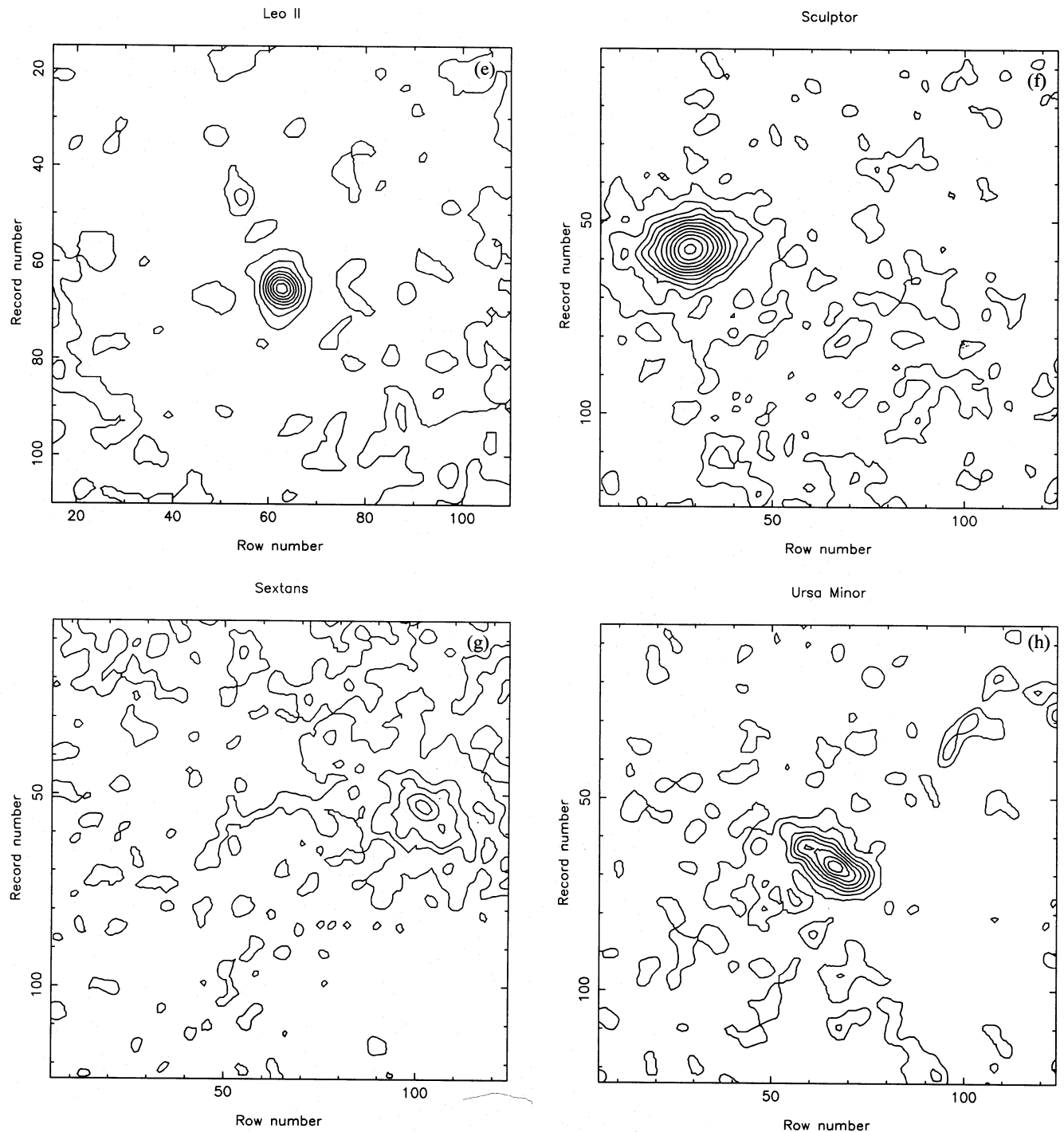


Figure 1 – continued

the red E plate was used) in these elliptical annuli are given together with the distance along the semimajor axis of the corresponding outer elliptical contour.

A fundamental problem in examining outer profiles of low-surface-brightness galaxies is the estimation of the 'true' background level. Overestimating the background contribution leads to artificially truncated light profiles, whilst underestimating the background produces an abnormally shallow galaxian profile with potentially non-convergent integral light. In our case, the 'background' consists of foreground

(Galactic) stars and background galaxies which together define the 'background' number density of images.

Three methods were used to estimate the 'background' density.

(1) The average number density of images over the whole region processed, with the dSph suitably excised, was measured.

(2) A Gaussian with its central level as a free parameter was fitted to the peak of the 'intensity' distribution from the

Table 2. The centres of gravity, mean ellipticities and mean position angles for the eight dSphs.

Galaxy	α, δ (B1950)	e	pa
Carina	6 ^h 40.6' –50°56'	0.33 ±0.05	65 ±5
Draco	17 ^h 19.5' +57°58'	0.29 ±0.01	82 ±1
Fornax	2 ^h 37.8' –34°41'	0.30 ±0.01	41 ±1
Leo I	10 ^h 05.8' +12°33'	0.21 ±0.03	79 ±3
Leo II	11 ^h 10.8' +22°26'	0.13 ±0.05	12 ±10
Sculptor	00 ^h 57.7' –33°59'	0.32 ±0.03	99 ±1
Sextans	10 ^h 10.5' –01°22'	0.35 ±0.05	56 ±5
Ursa Minor	15 ^h 08.4' +67°25'	0.56 ±0.05	53 ±5

isopleth map; the position of the peak of the Gaussian distribution then gives an estimate of the local ‘background’ contamination.

(3) Finally, the asymptotic value of the elliptical annuli number density at large radii was used to estimate the ‘background’ number density.

Generally, these separate (but not completely independent) methods produced values that agreed to within 1 per cent of the mean density of images. Our adopted values of the ‘background’ density with the corresponding error estimate are also given in Table 3. Fig. 2 shows the background-corrected number-density profiles (major axis) of the studied dSphs. A variable length average of successive annuli was used to keep the derived error bars (a combination of background error and Poissonian noise) roughly constant over the whole profile. There is a noticeable tendency for most of the dSphs to show an excess of stars, with respect to the best-fitting King model, at large radii. A similar effect was pointed out by Eskridge (1988a,c) for both Fornax and Sculptor. Eskridge notes that if his background estimates were set 3σ higher, then a better fit to exponential and King models ensues, but he emphasized that the background would then have to be higher than any plausible background fit. We find exactly the same effect with our data. In order to remove the apparent ‘extra-tidal’ stars (see also Section 7.4) the general background levels would have to be raised above any viable background estimate.

3 MODEL FITTING

In general, we might expect that at least some if not all dSphs have completed too few orbits around the Galaxy for their outer parts to have reached a tidally relaxed state and therefore that their observed limiting radii are determined by a combination of tidal effects and initial conditions. Nevertheless, isotropic single-component King models (King 1962, 1966) provide a tractable generic family of profiles that have been widely fitted to the observed density profiles of the dSphs (e.g. Hodge 1966; Eskridge 1988a,c). These models assume that all stars in the system have equal mass and are on radial orbits with a Maxwellian distribution of velocities that are tidally truncated by a dominant external mass (i.e. the system is a truncated isothermal sphere).

Several other model profiles have been used in the literature. Faber & Lin (1983) made use of exponential profiles and justified this approach by noting that extreme dwarf ellipticals are fitted as well by exponential profiles as by King models. Two-component King models – the two components representing dark and luminous matter with differing scale-sizes – have been used (e.g. Pryor & Kormendy 1990; Mateo et al. 1993) and other non-truncated isotropic models (Gaussian and Plummer) have been used, for example by Lake (1990).

In the following, we shall assume that the dSphs can be described by truncated isothermal spheres (King 1962, 1966). Essentially, by using single-component King models, we are also assuming that ‘mass follows light’ in these systems. These one-component King models are basically used as a means of parametrizing the structural characteristics of the dSphs. For comparison, we also show an exponential fit to all the radial profiles in Fig. 2, and list the derived exponential scalelengths (r_e) in Table 4. Although in general the exponential fits are significantly worse than King model fits, they provide a simple benchmark to compare with isolated dwarf ellipticals.

The free parameters of the models, i.e. the core (r_c) and tidal (r_t) radii and the central surface density (f_0) were derived by conventional χ^2 fitting of the models to the observed density profiles. The resulting derived values (along the major axis) of the core (r_c) and tidal radii (r_t) and their associated errors are given in Table 4. The quantities $r_{c,g}$, $r_{t,g}$, also given in Table 4, correspond to geometric means along the major and minor axes of the core and tidal radii, respectively. The concentration parameter [$c = \log(r_t/r_c)$] and the half-brightness radius, $r_{1/2,g}$ (geometric mean along the major and minor axes) are also given in the same table.

The best fits are overlaid on the logarithmic density profiles of Fig. 2. Apart from Sextans, King models produce a better overall fit than an exponential profile, suggesting that tidal interaction is a contributing factor in the determination of the outer shape of these dSphs.

The values derived, for the tidal radii in particular, are sensitive to the value adopted for the background density, discussed in Section 2.4. The errors quoted in Table 4 include this uncertainty. We note that, although theoretically attractive, the alternative parametrization of ‘core’ size in terms of the half-brightness radius ($r_{1/2}$) is somewhat difficult to achieve in practice. This arises mainly from the problem encountered in accurately estimating the central surface brightness without recourse to some sort of model fit. Conse-

Table 3. Star counts for the dSphs.

Carina									
r(')	d(no./'²)	r(')	d(no./'²)	r(')	d(no./'²)	r(')	d(no./'²)	r(')	d(no./'²)
0.66	9.73	17.90	3.34	35.14	2.96	52.38	2.46	69.61	2.82
1.33	11.89	18.56	3.14	35.80	3.17	53.04	2.64	70.28	2.86
1.99	13.18	19.23	3.03	36.47	2.54	53.70	2.89	70.94	2.77
2.65	8.03	19.89	3.06	37.13	2.73	54.37	2.67	71.60	2.68
3.32	10.33	20.55	3.54	37.79	3.18	55.03	2.78	72.27	2.76
3.98	10.22	21.22	2.98	38.45	2.93	55.69	2.85	72.93	2.79
4.64	10.14	21.88	2.96	39.12	2.99	56.35	2.87	73.59	2.72
5.30	8.43	22.54	2.87	39.78	3.09	57.02	2.76	74.26	2.78
5.97	7.25	23.20	3.57	40.44	3.05	57.68	2.75	74.92	2.65
6.63	7.45	23.87	3.20	41.11	2.85	58.34	2.78	75.58	2.83
7.29	7.10	24.53	3.17	41.77	2.55	59.01	2.75	76.24	2.91
7.96	7.61	25.19	3.18	42.43	2.43	59.67	2.81	76.91	2.90
8.62	6.70	25.86	3.05	43.09	3.02	60.33	2.88	77.57	2.78
9.28	6.20	26.52	2.89	43.76	2.80	61.00	2.88	78.23	2.76
9.94	6.04	27.18	2.84	44.42	2.72	61.66	2.77	78.90	3.00
10.61	5.93	27.85	2.90	45.08	2.83	62.32	2.99	79.56	2.98
11.27	5.14	28.51	2.91	45.75	2.74	62.99	2.44	80.22	2.62
11.93	5.06	29.17	2.96	46.41	2.74	63.65	2.91	80.89	2.75
12.60	4.67	29.83	3.02	47.07	2.94	64.31	2.83	81.55	2.94
13.26	4.10	30.50	2.60	47.74	2.72	64.97	2.95	82.21	2.95
13.92	3.90	31.16	2.79	48.40	2.65	65.64	2.86	82.88	3.08
14.59	4.35	31.82	2.90	49.06	2.84	66.30	2.65	83.54	2.85
15.25	4.37	32.49	3.09	49.72	2.97	66.96	2.68	84.20	2.76
15.91	3.70	33.15	2.94	50.39	2.97	67.63	2.75	84.86	3.02
16.57	3.37	33.81	2.69	51.05	2.59	68.29	2.80	0.00	0.00
17.24	3.33	34.48	2.92	51.71	2.58	68.95	2.99	0.00	0.00

Adopted background number density: $2.80 \pm 0.02 \text{ arcmin}^{-2}$.

Table 3 – continued

Draco									
r(')	d(no./'²)	r(')	d(no./'²)	r(')	d(no./'²)	r(')	d(no./'²)	r(')	d(no./'²)
0.49	11.37	13.23	2.61	25.96	1.61	38.70	1.57	51.43	1.73
0.98	6.32	13.72	3.10	26.45	1.77	39.19	1.91	51.92	1.95
1.47	8.34	14.21	2.89	26.94	1.95	39.68	1.66	52.41	1.65
1.96	11.92	14.69	2.31	27.43	2.00	40.17	1.76	52.90	1.87
2.45	7.79	15.18	2.27	27.92	2.18	40.66	1.85	53.39	1.76
2.94	6.20	15.67	2.56	28.41	1.80	41.15	1.69	53.88	1.94
3.43	7.44	16.16	2.62	28.90	1.99	41.64	2.06	54.37	1.80
3.92	6.32	16.65	2.15	29.39	2.20	42.13	2.48	54.86	1.81
4.41	7.14	17.14	1.95	29.88	2.04	42.62	1.82	55.35	2.02
4.90	8.08	17.63	2.40	30.37	2.07	43.11	2.21	55.84	2.05
5.39	5.69	18.12	2.10	30.86	2.14	43.60	2.25	56.33	1.96
5.88	6.76	18.61	2.20	31.35	1.49	44.08	1.99	56.82	1.85
6.37	6.14	19.10	1.92	31.84	1.81	44.57	1.78	57.31	2.05
6.86	5.55	19.59	1.99	32.33	1.97	45.06	1.96	57.80	1.92
7.35	4.45	20.08	2.22	32.82	1.85	45.55	1.95	58.29	1.86
7.84	5.08	20.57	2.22	33.31	1.52	46.04	1.74	58.78	1.79
8.33	4.83	21.06	2.14	33.80	1.72	46.53	1.85	59.27	2.10
8.82	4.66	21.55	1.77	34.29	1.92	47.02	2.33	59.76	1.97
9.31	3.79	22.04	2.07	34.78	2.10	47.51	1.94	60.25	2.11
9.80	3.31	22.53	2.23	35.27	1.96	48.00	1.98	60.74	2.06
10.29	4.12	23.02	1.88	35.76	2.05	48.49	2.07	61.23	2.18
10.78	4.01	23.51	2.18	36.25	1.81	48.98	1.59	61.72	1.90
11.27	3.67	24.00	1.95	36.74	1.27	49.47	1.77	62.21	2.02
11.76	3.59	24.49	1.90	37.23	2.00	49.96	1.84	62.70	2.04
12.25	2.90	24.98	2.18	37.72	1.47	50.45	1.78	0.00	0.00
12.74	3.09	25.47	2.17	38.21	2.01	50.94	1.75	0.00	0.00

Adopted background number density: $1.90 \pm 0.02 \text{ arcmin}^{-2}$.

Table 3 – continued

Fornax									
r(')	d(no./'²)	r(')	d(no./'²)	r(')	d(no./'²)	r(')	d(no./'²)	r(')	d(no./'²)
1.05	29.33	28.33	8.84	55.61	1.72	82.88	1.34	110.16	1.29
2.10	30.57	29.38	7.95	56.66	1.77	83.93	1.48	111.21	1.42
3.15	31.31	30.43	7.49	57.70	1.64	84.98	1.46	112.26	1.32
4.20	28.98	31.48	7.07	58.75	1.67	86.03	1.29	113.31	1.34
5.25	29.47	32.52	6.53	59.80	1.67	87.08	1.50	114.36	1.33
6.30	29.89	33.57	5.76	60.85	1.52	88.13	1.47	115.41	1.39
7.34	28.50	34.62	5.23	61.90	1.50	89.18	1.35	116.46	1.37
8.39	28.53	35.67	4.95	62.95	1.43	90.23	1.57	117.51	1.28
9.44	27.85	36.72	4.51	64.00	1.52	91.28	1.44	118.56	1.32
10.49	27.05	37.77	4.16	65.05	1.62	92.33	1.44	119.61	1.41
11.54	26.03	38.82	3.70	66.10	1.46	93.38	1.46	120.65	1.33
12.59	25.24	39.87	3.78	67.15	1.68	94.43	1.30	121.70	1.35
13.64	24.26	40.92	3.55	68.20	1.50	95.47	1.35	122.75	1.44
14.69	23.18	41.97	3.38	69.25	1.55	96.52	1.43	123.80	1.35
15.74	21.42	43.02	3.15	70.29	1.54	97.57	1.28	124.85	1.30
16.79	20.51	44.07	2.95	71.34	1.44	98.62	1.33	125.90	1.36
17.84	19.58	45.11	2.87	72.39	1.30	99.67	1.29	126.95	1.28
18.89	17.83	46.16	2.46	73.44	1.54	100.72	1.43	128.00	1.31
19.93	16.55	47.21	2.30	74.49	1.45	101.77	1.32	129.05	1.36
20.98	15.07	48.26	2.19	75.54	1.51	102.82	1.31	130.10	1.34
22.03	14.34	49.31	2.20	76.59	1.49	103.87	1.32	131.15	1.31
23.08	13.38	50.36	2.22	77.64	1.40	104.92	1.37	132.20	1.41
24.13	12.06	51.41	2.01	78.69	1.43	105.97	1.29	133.24	1.26
25.18	10.94	52.46	1.90	79.74	1.37	107.01	1.35	134.29	1.36
26.23	9.81	53.51	1.86	80.79	1.51	108.06	1.38	0.00	0.00
27.28	9.14	54.56	1.94	81.83	1.55	109.11	1.34	0.00	0.00

Adopted background number density: $1.34 \pm 0.01 \text{ arcmin}^{-2}$.

Table 3 – continued

Leo I									
r(')	d(no./'²)	r(')	d(no./'²)	r(')	d(no./'²)	r(')	d(no./'²)	r(')	d(no./'²)
0.33	18.32	8.95	1.80	17.58	1.74	26.20	1.28	34.82	1.38
0.66	15.88	9.29	1.67	17.91	1.58	26.53	1.20	35.16	1.23
0.99	18.32	9.62	1.48	18.24	1.21	26.86	1.23	35.49	1.20
1.33	16.75	9.95	1.43	18.57	1.22	27.20	1.42	35.82	1.23
1.66	18.73	10.28	1.38	18.90	1.30	27.53	1.24	36.15	1.37
1.99	14.32	10.61	1.63	19.24	1.40	27.86	1.25	36.48	1.29
2.32	13.81	10.94	1.18	19.57	1.66	28.19	1.43	36.81	1.44
2.65	12.46	11.28	1.26	19.90	1.54	28.52	1.18	37.15	1.07
2.98	12.07	11.61	1.65	20.23	1.12	28.85	0.97	37.48	1.17
3.32	9.26	11.94	1.60	20.56	1.34	29.19	1.30	37.81	1.13
3.65	9.25	12.27	1.51	20.89	1.23	29.52	1.22	38.14	1.46
3.98	8.60	12.60	1.17	21.23	1.10	29.85	1.04	38.47	1.43
4.31	7.33	12.93	1.71	21.56	1.62	30.18	1.34	38.80	1.54
4.64	5.84	13.27	1.25	21.89	1.31	30.51	1.92	39.14	1.12
4.97	5.05	13.60	1.81	22.22	1.40	30.84	1.27	39.47	1.25
5.31	4.73	13.93	1.02	22.55	1.52	31.18	1.06	39.80	1.47
5.64	5.11	14.26	1.64	22.88	1.18	31.51	1.32	40.13	1.35
5.97	3.98	14.59	1.35	23.22	1.50	31.84	1.25	40.46	1.19
6.30	2.77	14.92	2.02	23.55	0.99	32.17	1.37	40.79	1.39
6.63	3.10	15.26	1.97	23.88	1.18	32.50	1.18	41.13	1.36
6.96	2.68	15.59	1.65	24.21	1.19	32.83	1.32	41.46	1.09
7.30	2.64	15.92	1.35	24.54	1.27	33.17	1.45	41.79	1.11
7.63	2.77	16.25	1.51	24.87	1.60	33.50	1.64	42.12	1.48
7.96	3.20	16.58	1.30	25.21	1.04	33.83	1.25	42.45	1.26
8.29	2.39	16.91	1.67	25.54	1.63	34.16	1.27	0.00	0.00
8.62	1.58	17.25	1.28	25.87	1.23	34.49	1.22	0.00	0.00

Adopted background number density: $1.26 \pm 0.02 \text{ arcmin}^{-2}$.

Table 3 – *continued*

LeoII									
r(')	d(no./'²)	r(')	d(no./'²)	r(')	d(no./'²)	r(')	d(no./'²)	r(')	d(no./'²)
0.33	19.73	8.95	1.55	17.58	1.22	26.20	1.70	34.82	1.23
0.66	7.67	9.29	1.97	17.91	1.48	26.53	1.61	35.16	1.54
0.99	13.81	9.62	1.27	18.24	1.51	26.86	1.37	35.49	1.53
1.33	12.21	9.95	0.89	18.57	1.24	27.20	1.17	35.82	1.28
1.66	13.88	10.28	0.81	18.90	2.04	27.53	1.57	36.15	1.41
1.99	10.16	10.61	1.30	19.24	1.46	27.86	1.73	36.48	1.37
2.32	8.60	10.94	1.16	19.57	1.57	28.19	1.42	36.81	1.56
2.65	8.55	11.28	1.62	19.90	1.41	28.52	1.48	37.15	1.56
2.98	7.74	11.61	1.38	20.23	1.20	28.85	1.29	37.48	1.40
3.32	4.33	11.94	1.90	20.56	1.31	29.19	1.56	37.81	1.26
3.65	4.38	12.27	1.53	20.89	1.34	29.52	1.43	38.14	1.49
3.98	4.43	12.60	1.27	21.23	1.45	29.85	1.23	38.47	1.41
4.31	4.60	12.93	1.67	21.56	1.33	30.18	1.44	38.80	1.57
4.64	3.41	13.27	1.50	21.89	1.38	30.51	1.73	39.14	1.44
4.97	2.83	13.60	1.95	22.22	1.09	30.84	1.51	39.47	1.47
5.31	2.33	13.93	1.70	22.55	1.46	31.18	1.48	39.80	1.10
5.64	1.59	14.26	1.39	22.88	1.27	31.51	1.43	40.13	1.21
5.97	1.97	14.59	1.21	23.22	1.35	31.84	1.65	40.46	1.69
6.30	2.49	14.92	1.51	23.55	1.35	32.17	1.36	40.79	1.25
6.63	1.86	15.26	1.30	23.88	1.26	32.50	1.37	41.13	1.40
6.96	1.68	15.59	2.02	24.21	1.52	32.83	1.49	41.46	1.44
7.30	1.61	15.92	1.73	24.54	1.39	33.17	1.49	41.79	1.60
7.63	0.95	16.25	1.32	24.87	1.10	33.50	1.47	42.12	1.74
7.96	1.54	16.58	1.56	25.21	1.18	33.83	1.54	42.45	1.39
8.29	1.21	16.91	1.50	25.54	1.46	34.16	1.32	0.00	0.00
8.62	1.74	17.25	1.05	25.87	1.38	34.49	1.65	0.00	0.00

Adopted background number density: 1.44 ± 0.02 arcmin⁻².Table 3 – *continued*

Sculptor									
r(')	d(no./'²)	r(')	d(no./'²)	r(')	d(no./'²)	r(')	d(no./'²)	r(')	d(no./'²)
0.84	23.26	22.66	2.26	44.48	1.28	66.31	1.05	88.13	1.14
1.68	22.59	23.50	2.51	45.32	1.36	67.15	1.07	88.97	1.13
2.52	19.67	24.34	2.30	46.16	1.41	67.99	1.11	89.81	1.20
3.36	19.93	25.18	2.15	47.00	1.26	68.83	1.03	90.65	1.19
4.20	17.72	26.02	1.93	47.84	1.16	69.66	1.21	91.49	1.13
5.04	18.48	26.86	1.81	48.68	1.31	70.50	1.09	92.33	1.11
5.88	16.46	27.70	1.78	49.52	1.22	71.34	1.09	93.17	1.15
6.71	14.97	28.54	2.08	50.36	1.35	72.18	1.16	94.01	1.11
7.55	12.94	29.38	1.93	51.20	1.25	73.02	1.23	94.84	1.10
8.39	11.89	30.22	1.66	52.04	1.20	73.86	1.04	95.68	1.22
9.23	11.39	31.06	1.73	52.88	1.16	74.70	1.13	96.52	1.17
10.07	10.60	31.89	1.67	53.72	1.38	75.54	1.13	97.36	1.31
10.91	9.04	32.73	1.61	54.56	1.29	76.38	1.18	98.20	1.23
11.75	8.76	33.57	1.67	55.40	1.28	77.22	1.13	99.04	1.14
12.59	7.93	34.41	1.59	56.24	1.36	78.06	1.17	99.88	1.17
13.43	7.12	35.25	1.41	57.07	1.28	78.90	1.21	100.72	1.31
14.27	5.88	36.09	1.56	57.91	1.20	79.74	1.35	101.56	1.28
15.11	5.47	36.93	1.44	58.75	1.25	80.58	1.07	102.40	1.12
15.95	4.69	37.77	1.53	59.59	1.30	81.42	1.28	103.24	0.97
16.79	4.63	38.61	1.47	60.43	1.15	82.25	1.08	104.08	1.12
17.63	4.33	39.45	1.38	61.27	1.19	83.09	1.10	104.92	1.06
18.47	3.41	40.29	1.45	62.11	1.26	83.93	1.03	105.76	1.12
19.30	3.37	41.13	1.43	62.95	1.28	84.77	1.11	106.60	1.13
20.14	3.32	41.97	1.26	63.79	1.16	85.61	1.07	107.43	1.20
20.98	2.87	42.81	1.34	64.63	1.16	86.45	1.12	0.00	0.00
21.82	2.58	43.65	1.35	65.47	1.12	87.29	0.96	0.00	0.00

Adopted background number density: 1.13 ± 0.01 arcmin⁻².

Table 3 – continued

Sextans									
r(')	d(no./'²)	r(')	d(no./'²)	r(')	d(no./'²)	r(')	d(no./'²)	r(')	d(no./'²)
0.80	6.70	21.49	1.99	42.18	1.48	62.87	1.28	83.56	1.31
1.59	3.35	22.28	1.61	42.98	1.57	63.67	1.44	84.36	1.39
2.39	3.52	23.08	1.90	43.77	1.51	64.46	1.38	85.15	1.32
3.18	2.99	23.88	2.20	44.57	1.46	65.26	1.40	85.95	1.40
3.98	4.47	24.67	1.79	45.36	1.45	66.05	1.48	86.75	1.32
4.78	3.35	25.47	2.02	46.16	1.41	66.85	1.18	87.54	1.33
5.57	3.80	26.26	1.80	46.95	1.81	67.65	1.28	88.34	1.46
6.37	2.74	27.06	1.94	47.75	1.63	68.44	1.32	89.13	1.34
7.16	2.81	27.85	1.74	48.55	1.52	69.24	1.52	89.93	1.40
7.96	3.22	28.65	1.89	49.34	1.54	70.03	1.24	90.72	1.50
8.75	3.15	29.45	1.71	50.14	1.51	70.83	1.51	91.52	1.37
9.55	3.06	30.24	1.72	50.93	1.58	71.63	1.34	92.32	1.34
10.35	2.82	31.04	1.90	51.73	1.42	72.42	1.15	93.11	1.34
11.14	2.36	31.83	1.81	52.53	1.34	73.22	1.38	93.91	1.31
11.94	3.03	32.63	1.55	53.32	1.53	74.01	1.37	94.70	1.41
12.73	2.86	33.42	1.50	54.12	1.20	74.81	1.32	95.50	1.34
13.53	2.69	34.22	1.46	54.91	1.44	75.60	1.27	96.30	1.39
14.33	2.63	35.02	1.68	55.71	1.44	76.40	1.36	97.09	1.29
15.12	2.45	35.81	1.66	56.50	1.35	77.20	1.31	97.89	1.41
15.92	2.64	36.61	1.75	57.30	1.32	77.99	1.47	98.68	1.37
16.71	2.27	37.40	1.69	58.10	1.38	78.79	1.58	99.48	1.35
17.51	2.44	38.20	1.64	58.89	1.70	79.58	1.25	100.28	1.43
18.30	2.14	39.00	1.49	59.69	1.47	80.38	1.22	101.07	1.24
19.10	1.98	39.79	1.47	60.48	1.58	81.18	1.24	101.87	1.32
19.90	2.21	40.59	1.55	61.28	1.45	81.97	1.42	0.00	0.00
20.69	2.09	41.38	1.60	62.08	1.51	82.77	1.34	0.00	0.00

Adopted background number density: $1.34 \pm 0.02 \text{ arcmin}^{-2}$.

Table 3 – continued

Ursa Minor									
r(')	d(no./'²)	r(')	d(no./'²)	r(')	d(no./'²)	r(')	d(no./'²)	r(')	d(no./'²)
0.80	4.02	21.49	1.69	42.18	1.35	62.87	1.20	83.56	1.22
1.59	4.36	22.28	1.75	42.98	1.26	63.67	1.17	84.36	1.24
2.39	4.42	23.08	1.53	43.77	1.22	64.46	1.24	85.15	1.14
3.18	4.45	23.88	1.62	44.57	1.08	65.26	1.18	85.95	1.19
3.98	3.91	24.67	1.52	45.36	1.01	66.05	1.40	86.75	1.19
4.78	3.11	25.47	1.52	46.16	1.33	66.85	1.17	87.54	1.29
5.57	3.71	26.26	1.56	46.95	1.13	67.65	1.14	88.34	1.17
6.37	4.09	27.06	1.49	47.75	1.26	68.44	1.19	89.13	1.11
7.16	3.37	27.85	1.17	48.55	1.25	69.24	1.23	89.93	1.25
7.96	3.28	28.65	1.18	49.34	1.10	70.03	0.98	90.72	1.09
8.75	3.30	29.45	1.14	50.14	1.28	70.83	1.28	91.52	1.01
9.55	2.84	30.24	1.29	50.93	1.23	71.63	1.16	92.32	1.21
10.35	2.61	31.04	1.16	51.73	1.20	72.42	1.13	93.11	1.21
11.14	3.50	31.83	1.39	52.53	1.25	73.22	1.22	93.91	1.04
11.94	2.74	32.63	1.29	53.32	1.38	74.01	1.31	94.70	1.16
12.73	2.76	33.42	1.21	54.12	1.20	74.81	1.12	95.50	1.20
13.53	2.50	34.22	1.53	54.91	1.10	75.60	1.14	96.30	1.18
14.33	2.73	35.02	1.12	55.71	1.37	76.40	1.17	97.09	1.20
15.12	2.50	35.81	1.28	56.50	1.30	77.20	1.14	97.89	1.27
15.92	2.45	36.61	1.25	57.30	1.33	77.99	1.12	98.68	1.08
16.71	2.75	37.40	1.19	58.10	1.23	78.79	1.11	99.48	1.25
17.51	2.15	38.20	1.38	58.89	1.27	79.58	1.20	100.28	1.21
18.30	1.50	39.00	1.22	59.69	1.17	80.38	1.16	101.07	1.25
19.10	1.80	39.79	1.19	60.48	1.30	81.18	1.16	101.87	1.12
19.90	1.79	40.59	1.24	61.28	1.20	81.97	1.16	0.00	0.00
20.69	1.89	41.38	1.16	62.08	1.12	82.77	1.04	0.00	0.00

Adopted background number density: $1.16 \pm 0.01 \text{ arcmin}^{-2}$.

quently, $r_{1/2}$ is not better determined than r_c (cf. Lake 1990), since it essentially suffers from identical limitations.

For the transformation of the values of the tidal and core radii to physical dimensions (Table 4), we rederived the distance moduli for all dSphs using the observed (and dereddened) horizontal-branch magnitudes (except for the case of Leo I, where this value is not well known) and transforming these to absolute magnitudes using the relation by Carney, Storm & Jones (1992), $\langle M_V(RR) \rangle = 0.15(\pm 0.01)[Fe/H] + 1.01(\pm 0.08)$. These moduli are given in Table 5. Alternatively, the distance scale derived by Walker (1992) could be used. This would only change the value of the constant in the above equation, introducing just a systematic shift in the distance moduli.

As can be seen in Fig. 2, with the exception of the outermost regions of the dSphs, the models fit the observations quite well. The excess of stars with respect to the models in the outer regions of the dSphs could be either caused by an unexplained underestimation of the background density, or by the presence of 'extra-tidal' stars, or could simply denote that single-component King models are not a good approximation for the outer regions of the dSphs. These possibilities are discussed in Section 7.4.

4 MAGNITUDES AND CENTRAL SURFACE BRIGHTNESS

The integrated magnitudes of Carina, Draco, Sextans and Ursa Minor were derived from the photographic blue data by direct integration using the following steps. First, the King-model fit was used to define a region containing 90 per cent of the expected integral flux – a stand-off between both sampling the dSph adequately to reduce the Poissonian noise and keeping model extrapolation to a minimum, and the necessity of minimizing the chances of encountering bright 'background' stars. This region typically extends to $\frac{1}{2}$ the tidal radius. Secondly, the integral flux within this region, from the plate limit to the brightest stars in the dSph, was computed. Thirdly, multiple similarly sized background regions were randomly chosen and the integral flux within each was estimated. Finally, the median background flux was subtracted from the region centred on the dSph, and the variation in background fluxes used to estimate the likely error on the resultant dSph magnitude. A colour correction of $B_J - V = 0.5$ was subsequently applied (following Mateo et al. 1991) to convert to a visual integrated magnitude. Because of the relatively bright magnitude limit of the photographic

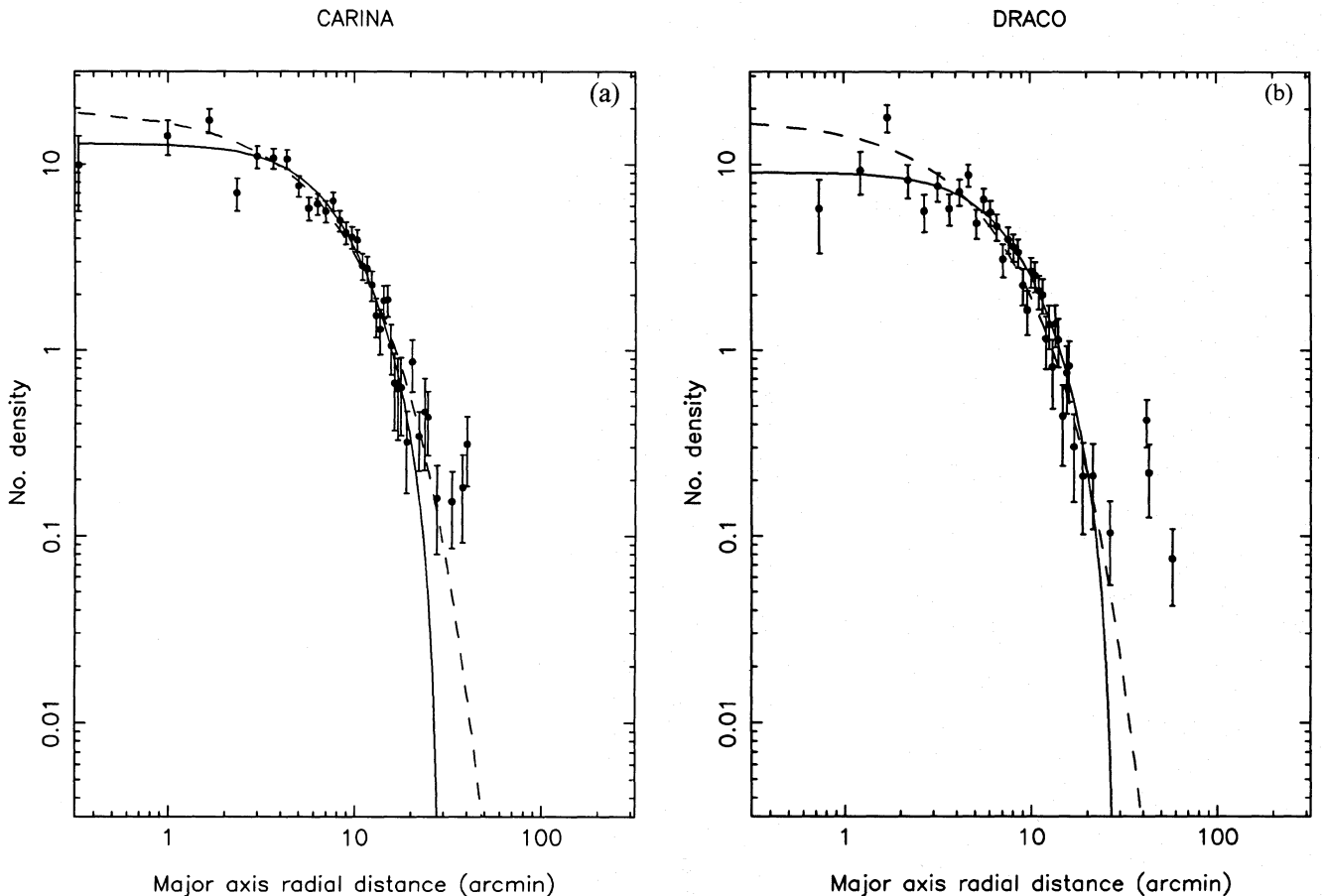


Figure 2. Major axis image number density radial profiles of the dSphs after correcting for both image crowding and contaminating 'background' images for: (a) Carina; (b) Draco; (c) Fornax; (d) Leo I; (e) Leo II; (f) Sculptor; (g) Sextans; and (h) Ursa Minor. The solid line is the best-fitting King-model profile, while the dashed line is the best-fitting exponential profile. In all cases apart from Sextans, the King profile gives a better fit, however, the radial profile of Sextans is indistinguishable from an exponential over the complete range. Note also the general presence of stars beyond the model-fit tidal cut-off. These 'extra-tidal' stars are particularly prominent for Fornax and Sculptor.

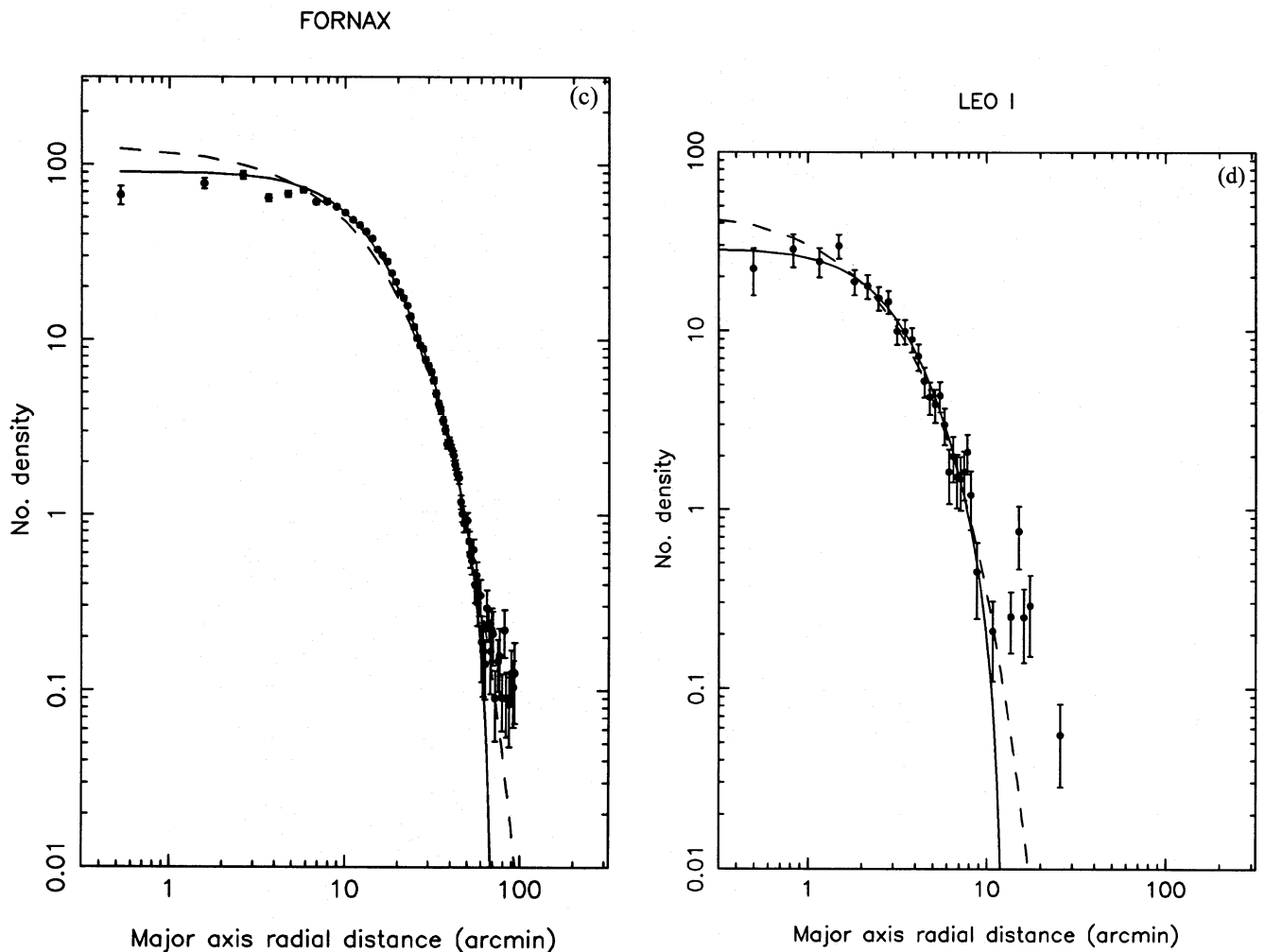


Figure 2 – continued

plates, some correction is essential to account for the fainter stellar population. This correction depends to first order on the slope of the luminosity function (LF) at the plate limit and lies in the range 0.1–0.5 mag, according to Mateo et al. We have adopted a fixed correction of 0.3 ± 0.2 mag. Table 6 shows the resulting integrated apparent visual magnitudes M_V with the associated combined errors.

In the cases of Fornax, Sculptor, Leo I and Leo II, this method could not be reliably applied: in the two former cases this was because of the large central densities causing significant image blending and in the latter two cases it was because of the strong effect of small number statistics. For Fornax, Leo I and Leo II, we estimated the integrated magnitudes using luminosity functions obtained from deep 4-m plates and CCD images (from Demers, Irwin & Kunkel 1994; Demers & Irwin 1993; Demers et al. 1993). The resulting integrated magnitudes are also shown in Table 6. In the case of Sculptor, no such data were available. We therefore adopted the value of Caldwell et al. (1992), which is based on the photoelectric surface brightness measured by Hodge & Smith (1974).

The central surface brightness is difficult to estimate directly, given the generally low central number densities of

these systems (especially at the photographic magnitude limit). The method that we applied involves the integration of the appropriate King model (with parameters from Table 4), and the use of the integrated magnitude evaluated above. The resulting estimates of the central surface brightness are also given in Table 6. A comparison of our luminosity and central surface brightness estimates with those of other authors is presented in Table 7. Considering the difficulty of the problem, the agreement is generally very good.

5 TWO-DIMENSIONAL DISTRIBUTION

Eskridge (1988b,d) claimed to have detected asymmetric structures in the 2D stellar distribution of Sculptor and Fornax. Although the interpretation of these structures is not clear, it is worth investigating whether similar asymmetries can be detected in the present data for Fornax and Sculptor, and the other six dSphs studied.

From direct inspection of the isopleth maps shown in Fig. 2, it is clear that little can be said regarding Leo I and II owing to their much greater distance. Likewise, the surface density of stars in Sextans is so low that the cell count noise dominates the map, making signs of asymmetry impossible to

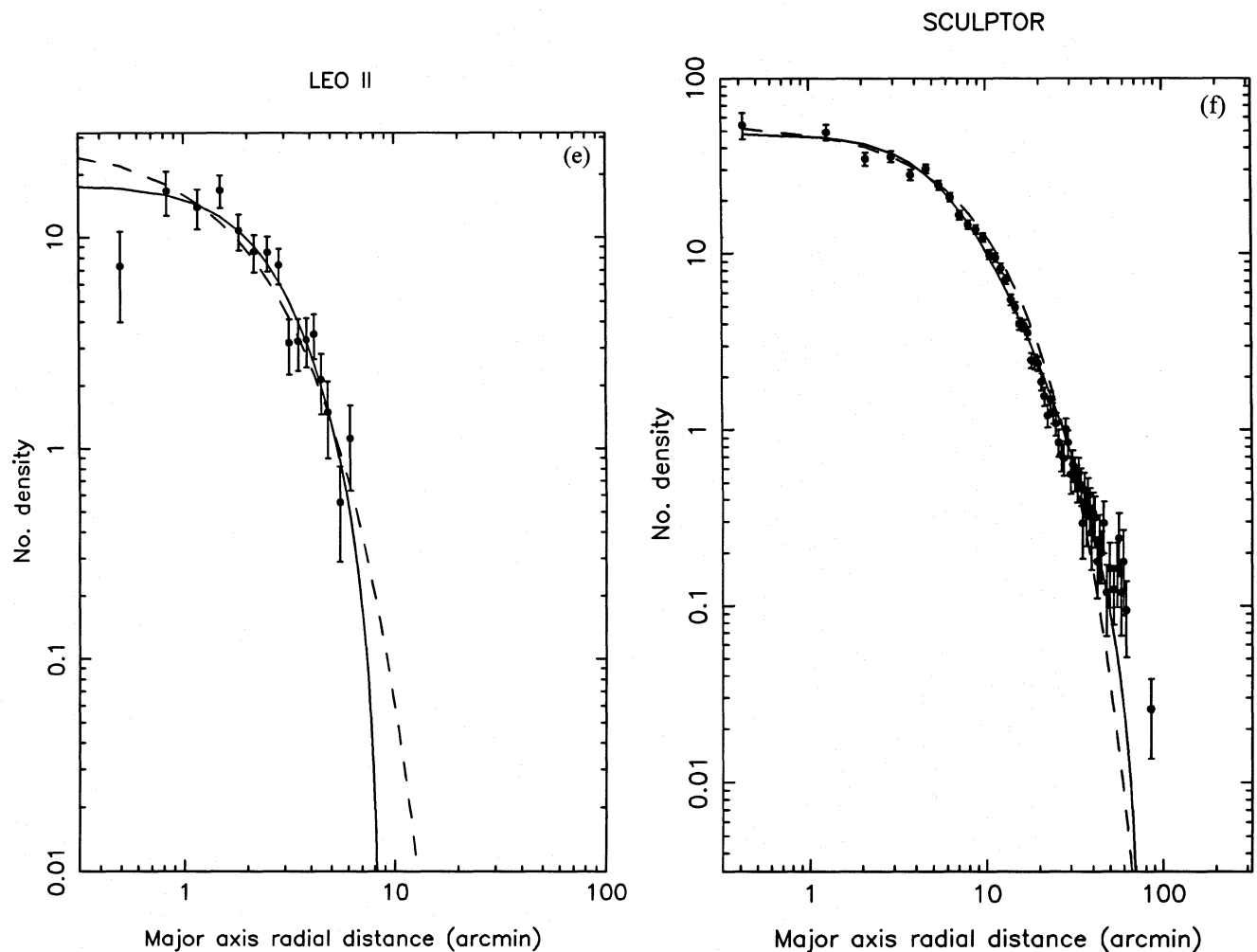


Figure 2 – continued

detect. For the other dSphs the situation is not as clear cut. Therefore, in order to quantify the degree of asymmetry, a similar method to that described by Eskridge was employed. The observed radial profile in conjunction with the global mean ellipticity and position angle were used to construct idealized 2D elliptical profiles for each dSph which were then subtracted from the isopleth maps shown in Fig. 2. Three of the dSphs: Fornax, Sculptor and Ursa Minor showed significant residual structure after this processing and the ‘difference’ isopleth maps for them are shown in Fig. 3. These maps are qualitatively similar to the ones produced by Eskridge (1988b,d) for Sculptor and Fornax.

In the case of Fornax, there is a significant asymmetry in the whole of the inner profile – in the sense that the contours are more closely spaced on the east side of the major axis than on the west (this effect was also noted by Hodge 1961a). This cannot be due to the five known globular clusters, since on UKST plates these are heavily saturated and contribute little to the local number counts. On the difference map, the asymmetry shows up as an excess of images to the south-east of the centre and a corresponding deficit to the north-west. Deeper photographic data derived from CTIO 4-m plates (Demers et al. 1994) reveals this asymmetry in more detail

and shows that it is centred on cluster 4. Indeed, cluster 4 appears to define the centre of Fornax. Apart from this large-scale asymmetry and the known clusters, there is no indication of any other significant residual structure with dimensions similar to the known clusters on either the 4-m or the UKST data (see also Demers et al. 1995).

As noted in Section 2.3, whilst analysing the global ellipticity as a function of radial distance for Sculptor (and Fornax), a tendency for the ellipticity to decrease with decreasing radius was noted. In the case of Sculptor, this trend is readily apparent in the direct isopleth map. The ‘difference’ isopleth map shows the effect very clearly. The central 10 arcmin of Sculptor (i.e. the core) has zero ellipticity. Outside this region, the ellipticity smoothly increases to the asymptotic mean value. Again there is no evidence for smaller scale structures. It is notable that Sculptor, with a circular core, an increasing ellipticity with radius and an excess of images at large radii, looks remarkably similar to numerical simulations of dSph galaxies that are tidally distorted. The preliminary proper motion for Sculptor announced recently by Schweitzer & Cudworth (1995) is consistent with orbital motion along the major axis and is exactly what would be expected for tidal distortion arising

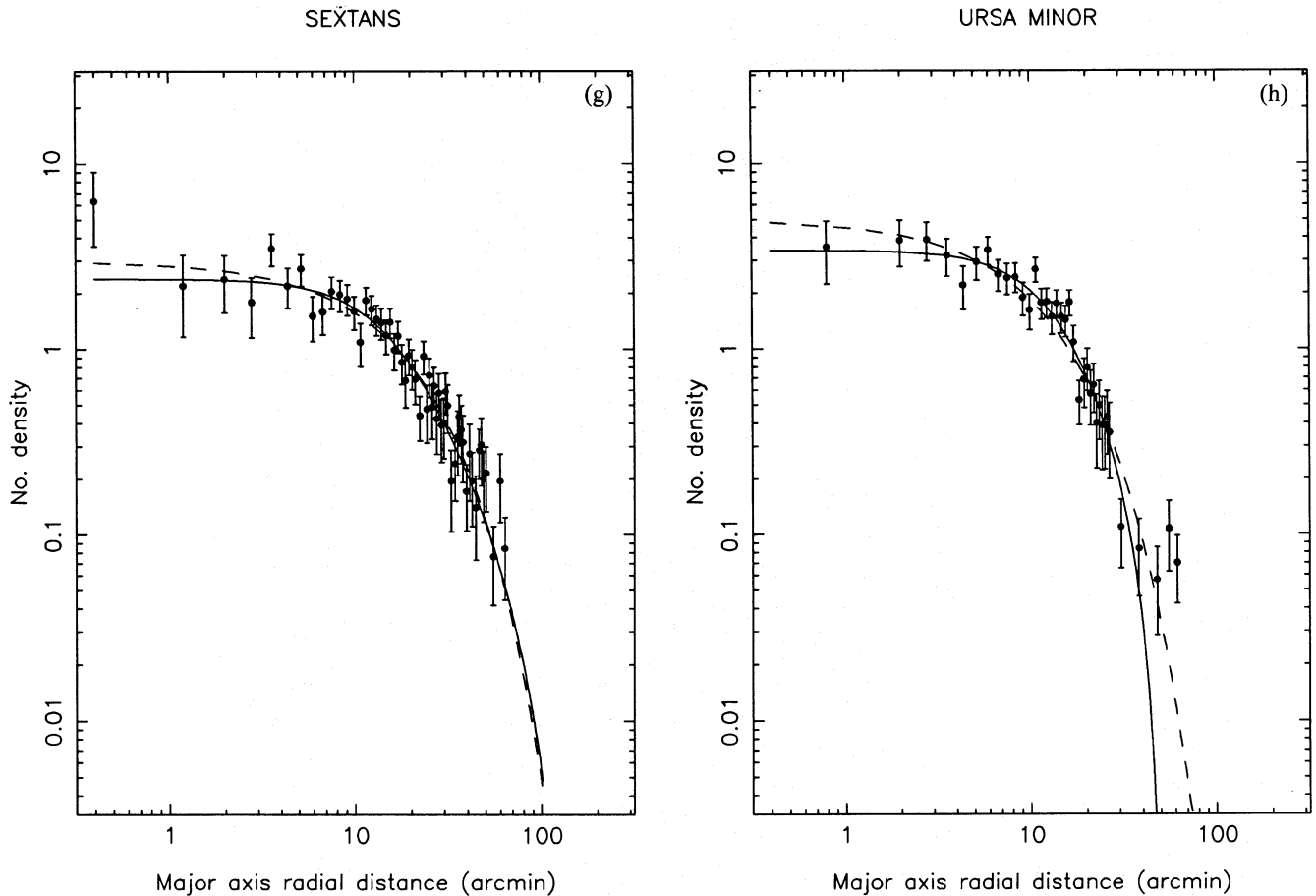


Figure 2 - continued

Table 4. Physical properties.

Galaxy	r_e (arcmin)	r_c (arcmin)	r_t (arcmin)	$r_{c,g}$ (pc)	$r_{t,g}$ (pc)	c	$r_{1/2,g}$ (pc)
Carina	5.5	8.8 ± 1.2	28.8 ± 3.6	177 ± 28	581 ± 86	0.51 ± 0.08	137 ± 22
Draco	4.5	9.0 ± 0.7	28.3 ± 2.4	158 ± 14	498 ± 47	0.50 ± 0.05	120 ± 11
Fornax	9.9	13.7 ± 1.2	71.1 ± 4.0	400 ± 43	2078 ± 177	0.72 ± 0.05	339 ± 36
Leo I	2.0	3.3 ± 0.3	12.6 ± 1.5	169 ± 19	645 ± 87	0.58 ± 0.07	133 ± 15
Leo II	1.5	2.9 ± 0.6	8.7 ± 0.9	162 ± 35	487 ± 60	0.48 ± 0.10	123 ± 27
Sculptor	6.8	5.8 ± 1.6	76.5 ± 5.0	101 ± 28	1329 ± 107	1.12 ± 0.12	94 ± 26
Sextans	15.5	16.6 ± 1.2	160.0 ± 50.0	322 ± 42	3102 ± 1028	0.98 ± 0.14	294 ± 38
Ursa Minor	10.1	15.8 ± 1.2	50.6 ± 3.6	196 ± 24	628 ± 74	0.51 ± 0.05	150 ± 18

from orbital motion. If the main phase of this tidal distortion occurred at the previous perigalactic passage $\sim 10^8$ yr ago, then Sculptor could be well on its way to being disrupted by the Galactic tidal field.

Olszewski & Aaronson (1985) were the first to note that Ursa Minor appeared to have two main clumps of stars spaced along the major axis. At the resolution of the isopleth maps shown in Fig. 2, these two clumps are just apparent and also show up on the 'difference' map in Fig. 3. We have further checked the reality of this feature on other Schmidt plates and have confirmed, using the automated APM morphological classifier, that the excess images are stellar in appearance. The separation between the clumps is ~ 15 arcmin. Their size is difficult to estimate from the low effective resolution of our isopleth maps, but they are probably not more than a few arcmin in diameter. A more detailed deep CCD study of the core region of Ursa Minor by Demers et al. (1995) found a clump of stars near the centre of the galaxy of diameter 2 arcmin, but did not extend far enough from the centre to investigate the secondary clump. Demers et al. found no other evidence for non-random clumps of stars (other than the known clusters in Fornax) in the central regions of Leo I, Leo II, Fornax, Ursa Minor and Draco.

Table 5. The distance moduli for all dSphs from observed horizontal-branch magnitudes.

Galaxy	V_{HB}	$E(B-V)^1$	Ref ²	$[Fe/H]^3$	$(m-M)_0$	$d(kpc)$
Carina	20.50 ± 0.10	0.025 ± 0.01	Mould & Aaronson 1983	-1.52 ± 0.20	19.64 ± 0.15	85 ± 5
Draco	20.07 ± 0.03	0.03 ± 0.01	Stetson 1979	-2.10 ± 0.20	19.28 ± 0.09	72 ± 3
Fornax	21.29 ± 0.06	0.03 ± 0.03	Buonanno <i>et al</i> 1985	-1.40 ± 0.20	20.40 ± 0.14	120 ± 8
Leo I	22.30 ± 0.10	0.00 ± 0.01	Demers <i>et al</i> 1993	-1.50 ± 0.30	21.48 ± 0.30	198 ± 30
Leo II	22.30 ± 0.10	0.00 ± 0.01	Demers & Irwin 1993	-1.90 ± 0.20	21.58 ± 0.13	207 ± 10
Sculptor	20.13 ± 0.02	0.02 ± 0.01	Kunkel & Demers 1977	-1.80 ± 0.20	19.30 ± 0.09	72 ± 5
Sextans	20.35 ± 0.20	0.02 ± 0.02	Mateo <i>et al.</i> 1991	-2.05 ± 0.20	19.59 ± 0.23	83 ± 9
Ursa Minor	19.80 ± 0.12	0.03 ± 0.03	⁴	-2.20 ± 0.20	19.04 ± 0.17	64 ± 5

¹An error of 0.01 in $E(B-V)$ was assumed, whenever no value was given in the literature.

²Studies from which both V_{HB} and $E(B-V)$ were taken.

³The values of $[Fe/H]$ were taken from Table 4 of Caldwell *et al.* (1992).

⁴The average of values given by Nemec *et al.* (1988), and Cudworth *et al.* (1986).

Table 6. Adopted luminosities.

Galaxy	M_V (mag)	L_{tot} (L_\odot)	Σ (mag/arcmin ²)	S_0 (L_\odot/pc^2)
Carina ¹	-8.6 \pm 0.5	(2.4 \pm 1.0) $\times 10^5$	16.6 \pm 0.5	2.2 \pm 1.0
Draco ¹	-8.3 \pm 0.5	(1.8 \pm 0.8) $\times 10^5$	16.6 \pm 0.5	2.2 \pm 1.0
Fornax ²	-13.0 \pm 0.3	(1.4 \pm 0.4) $\times 10^7$	14.4 \pm 0.3	15.7 \pm 5.1
Leo I ³	-11.5 \pm 0.3	(3.4 \pm 1.1) $\times 10^6$	13.7 \pm 0.3	30.9 \pm 10.0
Leo II ³	-9.6 \pm 0.3	(5.9 \pm 1.8) $\times 10^5$	15.3 \pm 0.3	7.8 \pm 2.5
Sculptor ⁴	-10.7 \pm 0.5	(1.4 \pm 0.6) $\times 10^6$	14.6 \pm 0.5	14.2 \pm 6.7
Sextans ¹	-9.2 \pm 0.5	(4.1 \pm 1.9) $\times 10^5$	18.2 \pm 0.5	0.7 \pm 0.3
Ursa Minor ¹	-8.4 \pm 0.5	(2.0 \pm 0.9) $\times 10^5$	17.1 \pm 0.5	1.5 \pm 0.7

¹Using photographic material from Table 1.

²From CTIO 4-m photographic plates (Demers *et al.* 1994).

³From CFH CCD data (Demers & Irwin 1993; Demers *et al.* 1993).

⁴Caldwell *et al.* (1992).

6 COMPARISON WITH PREVIOUS STUDIES OF DWARF SPHEROIDALS

In the past 30 years, several studies similar to the present one have been conducted with the purpose of deriving the structural parameters of the dSphs orbiting our Galaxy. The necessity of repeating these measurements has already been discussed in Section 1. Here, we compare the earlier estimates of r_c and r_t to our results. Table 8 lists all published derivations of r_c and r_t ; in some cases, the same original data were used by different authors to derive different values for the structural parameters. These occasions are clearly indicated.

In all cases, the semimajor axis values of r_c and r_t derived using the single-component King models (1962, 1966) are given (unless otherwise stated). It should also be pointed out that – as discussed in Section 4 – the King models do not fit the outer regions of the dSphs. This increases significantly the importance of the value used for the fore/background counts, in the derivation of r_t . It is again emphasized that these models are only used as a means of parametrizing the structure of these galaxies.

In most cases, the new values derived for r_c and r_t in the various studies agree, within the errors, with the previous measurements. For Fornax and Sculptor, the mean values of

Table 7. Summary of deviations of luminosities for dwarf spheroidal.

Reference	V	M _V	L (L _⊙)	Σ _{0,V} (mag/arcmin ²)	S ₀ (L _⊙ /pc ²)	Reference	V	M _V	L (L _⊙)	Σ _{0,V} (mag/arcmin ²)	S ₀ (L _⊙ /pc ²)
Carina											
Mateo <i>et al.</i> 1993 ¹ 2	10.8±0.3	-8.9	(3.1±0.8)×10 ⁵	16.3 16.7	3.0±1.0	Irwin <i>et al.</i> 1990 ¹⁵					
Webbink 1985 ³	10.74	-9.2	4.1×10 ⁵	17.1	1.4	Mateo <i>et al.</i> 1991 ¹⁶	10.3±0.7	-8.7±0.3	2.6×10 ⁵		1.3
Pryor 1992 ⁴	10.6	-9.2	4.1×10 ⁵	16.4	2.7	Caldwell <i>et al.</i> 1992 ¹⁷ present	10.2±0.5 10.4±0.5	-10.0 -9.2±0.5	8.6×10 ⁵ (4.1±1.9)×10 ⁵	16.6 18.2±0.5	1.5 0.7±0.3
Smecker-Hane <i>et al.</i> 1994 present	11.0±0.5	-8.6±0.5	(2.4±1.0)×10 ⁵	16.6±0.5	2.2±1.0	Ursa Minor					
Draco											
Webbink 1985 ⁵ Lake 1990 ⁶ present	10.78 11.0±0.5	-8.7 -8.3±0.5	2.6×10 ⁵ (1.8±0.8)×10 ⁵	16.3 16.6±0.5	2.9 4.5 2.2±1.0	Webbink 1985 ¹⁸ Lake 1990 ¹⁹ Caldwell <i>et al.</i> 1992 ²⁰ present	10.69 9.8±0.5 10.6±0.5	-8.7 -8.9 -8.4±0.5	2.6×10 ⁵ 3.1×10 ⁵ (2.0±0.9)×10 ⁵	16.4 16.2 17.1±0.5	2.6 4.1 3.2 1.5±0.7
Fornax											
Hodge 1971 Hodge & Smith 1974 de Vaucouleurs & Ables 1968	7.8 8.4	-13.6	2.4×10 ⁷	14.5 15.0		Sextans					
Buonanno <i>et al.</i> 1985 ⁷ Caldwell <i>et al.</i> 1992 ⁸ Pryor 1992 ⁹ present	6.9±0.5 7.4±0.3	-12.3±0.3 -13.7 -12.4 -13.0±0.3	7.1×10 ⁶ 2.6×10 ⁷ 7.8×10 ⁶ (1.4±0.4)×10 ⁷	14.3 14.8 14.4±0.3	18.4 15.7±5.1	Leo I					
Hodge 1971 Caldwell <i>et al.</i> 1992 ¹⁰ present	10.2±0.1 10.0±0.3	-11.4 -11.7 -11.5±0.3	3.1×10 ⁶ 4.1×10 ⁶ (3.4±1.1)×10 ⁶	13.4 13.7±0.3	42.1 30.9±10.0	Leo II					
Holmberg 1958 Hodge 1971 Hodge 1982 Vogt <i>et al.</i> 1995 present	12.0 11.62±0.25 11.6±0.3 12.0±0.3	-9.8 -10.2 -10.2±0.3 -9.6±0.3	7.1×10 ⁵ 10.3×10 ⁵ 9.9±3.2×10 ⁵ (5.9±1.8)×10 ⁵	17.64±0.18 ¹¹ 15.0±0.3 15.3±0.3	9.7±3.1 7.8±2.5	Sculptor					
Hodge 1971 Webbink 1985 ¹² Caldwell <i>et al.</i> 1992 ¹³ Pryor 1992 ¹⁴ present	8.13 8.8±0.5	-10.9 -11.4 -10.7 -10.7±0.5	2.0×10 ⁶ 3.1×10 ⁶ 1.6×10 ⁶ (1.4±0.6)×10 ⁶	14.55 15.2 15.0 14.6±0.5	14.6 8.0 9.4 14.2±6.7	Sextans					

¹They used the Demers *et al.* (1983) density profile and the luminosity function from Mighell (1990) and from Mateo & Nemec (private communication), assuming distance modulus of 19.7.

²Derived by us, by integrating the Mighell (1990) luminosity function.

³Based on Demers *et al.* (1983).

⁴Based on Demers *et al.* (1983) and assuming a distance modulus of 19.8.

⁵Based on the counts by Hodge (1964b) and using a fiducial luminosity function.

⁶Based on the counts and luminosity function by Hodge (1964b).

⁷Based on De Vaucouleurs & Ables (1968) and their newly derived distance modulus.

⁸Based on the Eskridge (1988c) density profiles, the Hodge & Smith (1964) photoelectric measurements.

⁹Averaging the Hodge & Smith (1974) and de Vaucouleurs & Ables (1968) measurements.

¹⁰Using the counts of Hodge (1963) and an empirical luminosity function derived for the Andromeda dwarf spheroidal.

¹¹Through a 20.2-arcsec aperture.

¹²Based on Hodge (1966).

¹³Based on the Eskridge (1988a) density profiles, the Hodge (1966) photoelectric measurements.

¹⁴Based on Webbink (1985).

¹⁵The estimate of the total magnitude does not include the contribution of stars fainter than the plate limit.

¹⁶The estimate was achieved through comparison of the number density of horizontal-branch stars in the central regions of Sextans and Sculptor.

¹⁷Using the Irwin *et al.* (1990) counts and an empirical luminosity function derived for the Andromeda dwarf spheroidal.

¹⁸Based on Hodge (1964a).

²⁰Using the Hodge (1964a) counts and an empirical luminosity function derived from the Andromeda dwarf spheroidal.

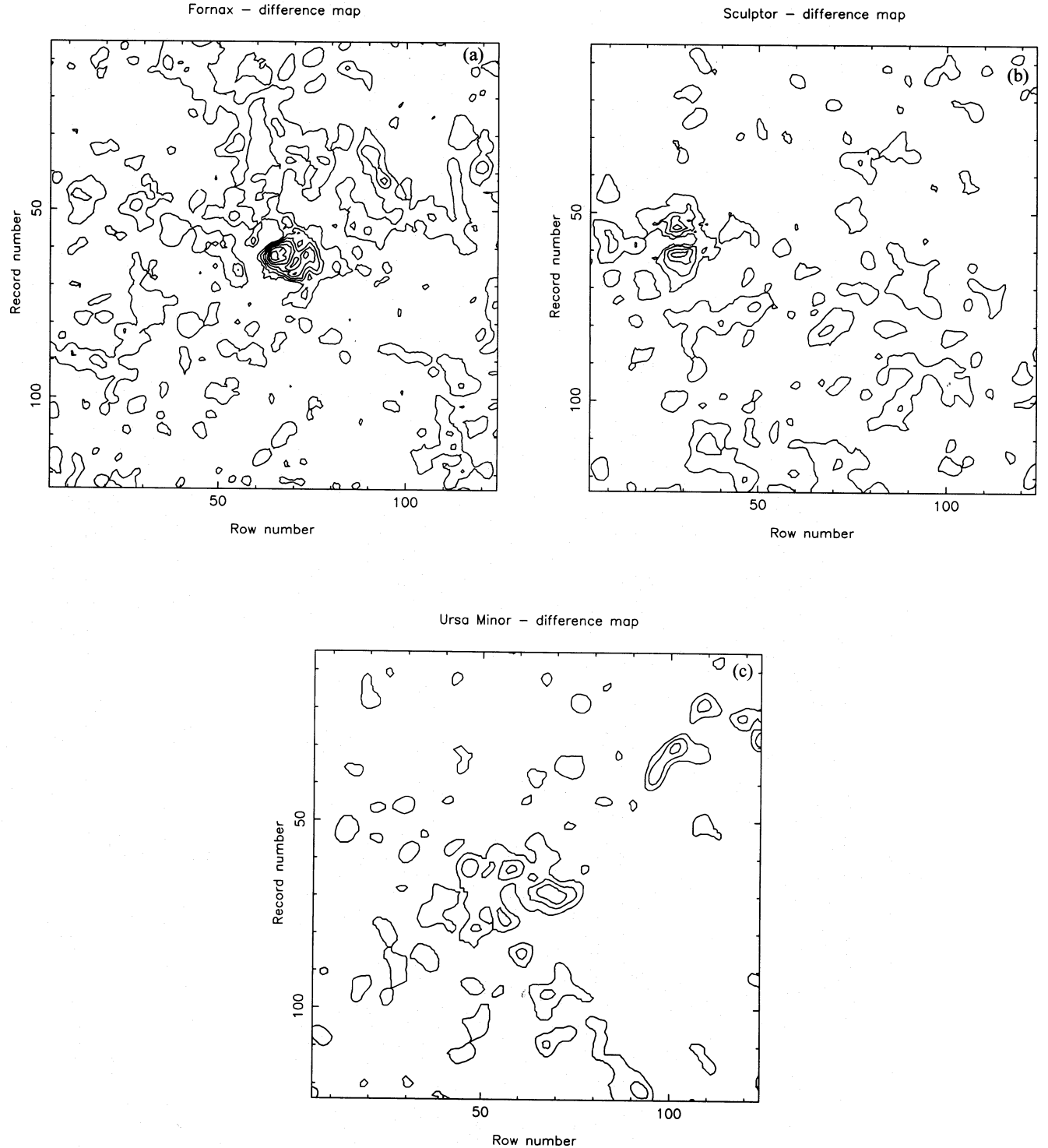


Figure 3. Three of the dSphs: (a) Fornax, (b) Sculptor and (c) Ursa Minor, show residual structure after a best-fitting smooth elliptical profile has been subtracted. The three difference isopleth maps shown in (a), (b) and (c) corresponding to Fornax, Sculptor and Ursa Minor respectively are plotted at the same orientation and with the same contour levels as for the equivalent maps shown in Fig. 1, apart from Ursa Minor where the contour spacing has been changed to 0.2 arcmin^{-2} to emphasize the double-peaked nature of the stellar distribution. Fornax shows striking irregularities in its central regions that, on closer inspection, are due to a general image density asymmetry in the central region centred on cluster 4. The difference map for Sculptor highlights the presence of a circular core with the ellipticity progressively increasing as a function of radius. This is also apparent by direct inspection of Fig. 1(f). However, apart from the known clusters of Fornax, neither Fornax nor Sculptor show any evidence of localized star clusters or clumps. Ursa Minor, on the other hand, appears to resolve into two general clumps of stars separated by some 15 arcmin along the major axis.

Table 8. Summary of structural derivations for dwarf spheroidals.

Reference	r_c arcmin	r_t arcmin	ϵ	p.a. deg
Carina				
Demers <i>et al</i> 1983	10.7	33.2	0.41 ± 0.04	75
Godwin 1985	9.6	47	0.31	72
present	8.8 ± 1.2	28.8 ± 3.6	0.33 ± 0.05	65 ± 5
Draco				
Hodge 1966	6.5	26 ± 2	0.29 ± 0.04	84 ± 3
Lake 1990 ³	$7^{+3}_{-2.5}$	55^{+30}_{-30}		
Pryor & Kormendy 1990 ⁴	7.1	36		
present	9.0 ± 0.7	28.3 ± 2.4	0.33 ± 0.05	82 ± 1
Fornax				
Hodge 1961a ¹	-	56	0.20-0.37	54
Hodge 1966	16	50 ± 6	0.20-0.37	54
Hodge & Smith 1974	14	76	0.27 ± 0.02	49 ± 2
de Vaucouleurs and Ables 1968	15-20	>60		
Godwin 1985	12.7	57	0.35	
Paltoglou & Freeman 1987 ²	17.7	56		
Eskridge 1988c	16.7 ± 1.8	108 ± 3	0.30 ± 0.02	40.2 ± 2.0
present	13.7 ± 1.2	71 ± 4	0.30 ± 0.01	41 ± 1
Leo I				
Hodge 1963	-	14.3 ± 1.0	0.31 ± 0.07	-
Hodge 1966	4.5	13.9 ± 0.5	0.31 ± 0.07	-
Godwin 1985 ³	4.3	13	0.31	-
present	3.3 ± 0.3	12.6 ± 1.5	0.21 ± 0.03	79 ± 3
Leo II				
Hodge 1962 ¹	-	11.9 ± 0.3	0.01 ± 0.01	-
Hodge 1966	2.5	9.6 ± 1.5	0.01 ± 0.01	-
Demers & Harris 1983	3.4	10.7	-	-
Godwin 1985 ³	2.28	10	0.01	-
present	2.9 ± 0.6	8.7 ± 0.9	0.13 ± 0.05	12 ± 10
Sculptor				
Hodge 1961b ¹	-	46 ± 3	0.35 ± 0.05	98 ± 2
Hodge 1966	11.9	53 ± 5	0.35 ± 0.05	98 ± 2
Innanen & Papp 1979	-	48	-	-
Demers <i>et al</i> 1980	7.5	≥ 75	0-0.3	-
Eskridge 1988a	8.9 ± 0.9	95 ± 10	0.34 ± 0.04	95.4 ± 4.3
present	5.8 ± 1.6	76 ± 5	0.32 ± 0.03	99 ± 1
Sextans				
Irwin <i>et al</i> 1990	15	90	0.4	56
present	16.6 ± 1.2	160.0 ± 50.0	0.35 ± 0.05	56 ± 5
Ursa Minor				
Hodge 1966	11.1	59 ± 25	0.55 ± 0.10	50 ± 4
Lake 1990 ³	$11^{+4.5}_{-2.5}$	59^{+30}_{-25}		
Pryor & Kormendy 1990 ⁴	12.4	31.3		
present	15.8 ± 1.2	50.6 ± 3.6	0.56 ± 0.05	53 ± 5

¹Using the King (1961) formulation.²Actual star counts remain unpublished.³Based on the star counts published by Hodge (1964a,b) and on Plummer-model fitting.⁴Based on the star counts published by Hodge (1964a,b) and for isotropic single-component King-model fitting. In the same paper, the authors fitted several other models to the observed density profiles.

the old estimates are significantly increased by the single very high value given by Eskridge (1988a,c). Since one of the plates used in the Eskridge study of Fornax, J8297, was the same as the one used in our analysis, we looked in more detail at the cause of the disagreement. In the background regions, at the notional tidal radius and beyond, we find almost identical object number densities, which indicates that the plates were measured to the same depth. However, in the centre of Fornax, Eskridge finds number densities lower by a factor of 3 than our crowding-corrected values. Indeed, his central number density agrees rather well with our uncorrected value. We have checked the crowding correction empirically by measuring CTIO 4-m plates centred on Fornax using the automatic crowded field software described by Irwin (1985). We find excellent agreement between our statistically corrected Schmidt-plate values and those derived from the equivalent magnitude-limited 4-m sample. Our conclusion is that, although Eskridge's sample was constructed using crowded field software, the latter was an early version, which in practice did not work well in the mix of resolved stars and unresolved background light making up the central part of Fornax. We believe that a similar problem also occurred with the Sculptor data. Therefore, given that the central density was significantly underestimated, it is hardly surprising that the derived core radii were too large and likewise the tidal radii were also overestimated.

Finally, the older estimates of the ellipticity ϵ and the position angle agree, within 2σ , in all cases with the new values of Table 2, except for Draco where there are significant deviations from the Hodge (1966) estimates.

The integrated magnitudes and central surface brightnesses of the dSphs estimated in previous studies are given in Table 7. In general, there is good agreement within the errors. A notable exception is the surface brightness of Sextans and Ursa Minor which are significantly lower according to our estimates. In the case of Leo II, there is also a large discrepancy with the value given by Hodge (1982). Although we have no independent way of confirming our lower central surface brightness for Sextans or Ursa Minor it is illustrative to examine the derived (from a King model fit) central number densities on the plate material used. All of the UKST B_J plates reach a similar limiting magnitude so, in particular, we can compare the central derived image density of Carina (12.9 arcmin^{-2}) and Sextans (3.2 arcmin^{-2}). With the caveats of differing stellar populations and slightly different distances, this suggests that Sextans has a central surface brightness some $1.5 \text{ mag arcsec}^{-2}$ fainter than Carina, in agreement with our fainter derivation of the central surface brightness of Sextans. Likewise, the plates used to study Ursa Minor and Draco also reach similar limiting magnitudes and the derived central surface densities are 3.5 arcmin^{-2} and 9.1 arcmin^{-2} respectively, suggesting Ursa Minor has a central surface brightness some 1 mag fainter than Draco. (Eyeball inspection of the Palomar-Sky-Survey plates supports this conclusion too.)

7 DISCUSSION

7.1 Derivation of mass-to-light ratios

The mass-to-light ratio in the central regions of the dSphs has been the subject of numerous investigations. It has often

been claimed (see Pryor 1992 for a review) that at least in some cases e.g. Draco, Ursa Minor and to a lesser extent, Carina, the gravitational potential is dominated by dark matter.

In this section we formally calculate the mass-to-light ratios for the eight dSphs studied in two different ways, assuming in both cases a single-component spherical system with an isotropic velocity distribution (and for the global M/L a truncated isothermal velocity distribution function). Finally, it is implicitly assumed (by using single-component modelling) that dark matter, if present, must have an identical spatial distribution to the luminous matter (or, equivalently, that mass follows light).

As noted earlier, dSphs are probably not in a dynamically relaxed state with regard to the tidal field of the Galaxy. However, the profiles presented in Fig. 2 show unambiguous evidence for the effects of tidal interaction, since the outer part of the profiles turn over more rapidly than the exponential profiles seen in isolated dwarf systems. Single-component King models therefore provide a useful benchmark for making further deductions regarding the dynamical properties of the dSphs.

More realistic dynamical models can be applied by introducing a certain amount of velocity anisotropy to the models, and/or by relaxing the assumption that mass follows light (see for example Mateo et al. 1993). The purpose of the estimation of the mass-to-light ratios presented here is to provide a comparative data base for the eight dSphs studied, rather than to present realistic models for their structure. Nevertheless, it is obvious that the data base given in Table 3, in conjunction with measurements of the dependence of the velocity dispersion with radius, can be used in future to explore more realistic models of the dSphs.

In the following two subsections, we first derive the 'global' mass-to-light ratio using the method described by Illingworth (1976), which is, strictly speaking, only applicable to single-component King models and clearly requires knowledge of the 'global' morphological properties of the dSphs. Secondly, the central mass-to-light ratio is calculated, based on the method outlined by Richstone & Tremaine (1986). In this case the profile is parametrized by the half-light radius ($R_{1/2}$); consequently a much wider range of single-component models are valid and the central M/L value does not depend so strongly on the sensitive measurement (and modelling) of the outer profile. We prefer the method of Richstone & Tremaine over that described by Kormendy (1987), since the latter method is just a special case (i.e. for a King model profile) of the former one. It must be emphasized that in all these methods it is assumed that the dSphs are in (or close to) dynamical equilibrium, otherwise the mass estimators used are not valid.

In estimating either the global or central M/L, knowledge of the central velocity dispersion of the system is required; Table 9 summarizes the best current estimates (and the corresponding references) of the velocity dispersions of the eight dSphs; the velocity dispersion of Leo I is still not well known.

All sources of error were taken into account when estimating the errors in the derived M/L ratios; this has not always been the case in previous publications, and as a result the values presented here often appear much more uncertain than previous measurements, although we attempted to use

Table 9. Adopted velocities.

Galaxy	V_0 (km/s) ¹	V_z (km/s) ²	σ_0 (km/s)	Reference
Carina	223 ± 1.8	7	6.8 ± 1.6	Mateo et al. 1993
Draco	-289 ± 1	-94	13.2 ± 2.1	Mateo et al. 1993
Fornax	53.0 ± 1.8	-36	11.0 ± 2.0	Mateo et al. 1993
Leo I	285 ± 2	177	3.2 ± 2.8^3	Suntzeff et al. 1986
Leo II	76.0 ± 1.3	22	6.7 ± 1.1^3	Vogt et al. 1995
Sculptor	107 ± 2	74	7.0 ± 1.2	Mateo et al. 1993
Sextans	224.4 ± 1.6	73	7.0 ± 1.1^4	Hargreaves et al. 1994a
Ursa Minor	-250 ± 1	-88	7.5 ± 1.0^5	Hargreaves et al. 1994b

¹The heliocentric radial velocities V_0 of Draco, Leo I, Sculptor and Ursa Minor are taken from Zaritsky et al. (1989); that of Fornax from Mateo et al. (1991); that of Carina from Mateo et al. (1993); that of Sextans from Hargreaves et al. (1994a; see also note 3); that of Leo II from Vogt et al. (1995).

²The galactocentric radial velocity V_z is derived using a velocity vector of (9, 232, 7) km s⁻¹ for the solar motion with respect to the Galactic Centre.

³The velocity dispersion and associated error for Leo I shown here corresponds to the possible range of velocity dispersion values rather than the actual mean value and associated 1-sigma error. It was derived from the observation of too few stars and with insufficient velocity accuracy, and therefore it is much more uncertain than the values given for the other dSphs.

⁴From multiple observations of 26 stars, with individual velocity accuracy of 2 km s⁻¹.

⁵From multiple observations of 46 stars, with individual velocity accuracy of 2 km s⁻¹.

the best current data on distances (Table 5), velocity dispersions (Table 9) and structural parameters (Table 4). Although we have quoted an rms error, the probability distribution function for the derived M/L is generally asymmetric and far from being even approximately Gaussian.

7.1.1 Derivation of the global M/L ratio

Assuming a single-component King model, the total mass-to-light ratio of the system can be calculated by applying the method of Illingworth (1976), where

$$\frac{M_{\text{tot}}}{L_{\text{tot}}} = \frac{166.5 r_{c,g} \mu}{\beta L_{\text{tot}}} \quad (1)$$

using the notation of Hargreaves et al. (1994a). The mass-to-light ratio thus derived is in solar units; $r_{c,g}$ is the King core radius of the system in pc (geometric mean along the major and minor axes); μ is the King dimensionless mass parameter (King 1966), which depends on the central concentration c of the model used; β is a model-dependent parameter which is related to the observed velocity dispersion and the projected distance r from the centre (see fig. 4.11 in Binney & Tremaine 1987). The correction to the observed velocity dispersion is significant for relatively low-concentration models such as the ones appropriate for the

dSphs. We have applied the correction at $r=r_c$, since most of the stars with observed line-of-sight velocities lie close to the core region.

Table 10 gives the values of μ , of $\sqrt{\beta\sigma^2}$ and of the derived global mass and mass-to-light ratios with associated errors. The reader will notice that these errors are still disappointingly large, although we have used the best available estimates of all relevant quantities. It is interesting to investigate the major source of these errors: in the case of Draco, Sculptor, Sextans and Ursa Minor the major source of error is L_{tot} ; in the case of Leo I, Fornax and to a lesser extent of Carina, the velocity dispersion is the main culprit, while in the case of Leo II, the error in μ accounts for most of the error in M/L . This error was not taken into account in the most recent determination of M/L of Leo II by Vogt et al. (1995).

7.1.2 Derivation of the central M/L ratio

The central mass-to-light ratio can be calculated using the core-fitting technique, described by Richstone & Tremaine (1986). The central mass-to-light ratio (in solar units) is given by

$$\frac{\rho_o}{I_o} = \eta \frac{333\sigma_o^2}{r_{1/2}S_o}, \quad (2)$$

where σ_o is the 'central' velocity dispersion (in km s^{-1}), $r_{1/2}$ is the half-brightness radius (in pc) (geometric mean along the minor and major axes), η is a factor depending on the dynamical model assumed, and was calculated for the King models by Richstone & Tremaine and S_o is the central surface brightness (in $L_\odot \text{ pc}^{-2}$). For a King model only, the central mass density is given by

$$\rho_o = \frac{166.5}{\beta r_c^2}. \quad (3)$$

With the concentration parameters appropriate for the dSphs ($0.5 < c < 1.1$, e.g. Table 4), η ranges from 0.955 to 0.98. The values adopted for each case are shown in Table 10, but it is obvious that the resulting value of ρ_o/I_o is not sensitive to the typical range of η . Since the stars from which the velocity dispersion is measured do not actually lie in the centre of the dSph, the observed velocity dispersion must be corrected accordingly. Again, we applied the appropriate correction (from fig. 4.11 of Binney & Tremaine 1987) at $r=r_c$. This correction is tabulated in Table 10 along with the estimates of ρ_o and ρ_o/I_o . This method is less model dependent than the one described in Section 7.1.1. The percentage errors of ρ_o/I_o are slightly lower than those of the global mass-to-light ratios. Again it is interesting to note that the major contribution to these errors come from the error in the velocity dispersion for Carina, Fornax, Leo I and Leo II, and from the error in the central surface brightness for Draco, Sculptor, Sextans and Ursa Minor. On no occasion does the error in $r_{1/2}$ have a significant contribution to the total error budget.

7.1.3 Dark matter in the dSphs

Even though the uncertainties quoted for the mass-to-light ratios in Table 10 should only be taken as indicative of 1σ errors (the underlying probability distribution is non-Gaussian and asymmetric), it is clear that none of the dSphs individually show incontrovertible evidence for $M/L \gg 1$. The errors remain large, despite the fact that we used the best available data for the various quantities involved in the

Table 10. Mass-to-light ratios.

Galaxy	μ	$\sqrt{\beta\sigma_{\text{obs}}^2}$	M ($10^6 M_\odot$)	M/L (M_\odot/L_\odot)	η	$\sigma_{\text{obs}}/\sigma_o$	ρ_o ($M_\odot \text{ pc}^{-3}$)	ρ_o/I_o (M_\odot/L_\odot)
Carina	2.8 ± 1.3	0.52	14.1 ± 10.0	59 ± 47	0.955	0.81	0.91 ± 0.45	74 ± 50
Draco	2.6 ± 0.8	0.52	44.1 ± 24.0	245 ± 155	0.955	0.80	4.3 ± 1.4	328 ± 184
Fornax	6.0 ± 0.8	0.7	98.7 ± 42.0	7 ± 3	0.965	0.86	0.26 ± 0.10	10 ± 4
Leo I	3.8: ± 1.1	0.59	3.1:	0.9:	0.960	0.83	0.17:	1.2:
Leo II	2.3 ± 1.7	0.45	13.8 ± 7.9	23 ± 20	0.955	0.80	1.4 ± 0.7	23 ± 11
Sculptor	14.0 ± 2.6	0.87	15.2 ± 7.7	10.9 ± 7.5	0.980	0.93	1.1 ± 0.4	14 ± 9
Sextans	11.2 ± 3.0	0.82	43.8 ± 23.6	107 ± 72	0.980	0.91	0.12 ± 0.05	94 ± 42
Ursa Minor	2.8 ± 0.8	0.52	19.0 ± 10.5	95 ± 43	0.955	0.81	0.90 ± 0.40	121 ± 66

calculations. However, considered as an ensemble, the values for both the central and the global mass-to-light ratios of the dSphs, taken at face value, suggest the possible presence of significant amounts of dark matter in Draco, Ursa Minor, Sextans and Carina.

Large values for the mass-to-light ratios have also previously been found for Ursa Minor and Draco (e.g. Pryor 1992), Carina (Mateo et al. 1993), Sextans (Hargreaves et al. 1994a) and Leo II (Vogt et al. 1995). As pointed out by many other authors there is a notable apparent inverse trend of mass-to-light ratio with luminosity. Indeed the four lowest luminosity systems have the highest apparent mass-to-light ratio. This is consistent with the trend predicted by Dekel & Silk (1986) on the basis of assuming the universal presence of dark-matter haloes.

However, one has to keep in mind the underlying assumptions in the methodology followed here (and by many other authors) for the calculation of these mass-to-light ratios (see also Vogt et al. 1995), namely that the mass distribution follows the distribution of the visible matter, that the stellar orbits are isotropically distributed and that the systems are in dynamical near-equilibrium. One way for this last assumption to be invalid is discussed in Section 7.4. A further problem is the unknown contribution to the observed velocity dispersion from binary systems. For example, Suntzeff et al. (1993) point out that a binary fraction of 25 per cent is sufficient to explain away the observed high velocity dispersion in Sextans. A similar binary contamination in the other dwarf spheroidals cannot yet be ruled out with the currently available observational data.

It is clear that the question of the presence of dark matter in dSphs is far from settled satisfactorily yet.

7.2 The perigalactic distances of the dSphs

As we noted earlier, it is not clear whether the dSphs have undergone enough orbits to be considered to be in dynamical equilibrium with the Galactic tidal field. However, for the following discussion we shall assume that the dSphs are tidally truncated by the gravitational field of our Galaxy in order to investigate their susceptibility to tidal distortion and eventual tidal disruption.

Using the formula for the tidal radius in a point mass potential from King (1962), the approximate perigalactic distance for a tidally truncated satellite is

$$D_{pg} = r_t \left[\frac{(3+e)M_G}{M} \right]^{1/3}, \quad (4)$$

where M_G is the mass of the Galaxy, D_{pg} is the perigalactic distance of the satellite, M its mass, r_t its tidal radius and e the eccentricity of its orbit. As mentioned by Faber & Lin (1983), the Galaxy potential is softer than that of a point mass, and a correcting factor of $(2/3)^{-1/3}$ is needed to account for this effect. This correction can obviously be absorbed in the value used for the mass of the Galaxy. Using the radial velocities of globular clusters and dSphs and assuming the point mass approximations of Lynden-Bell, Cannon & Godwin (1983) and isotropic orbit distributions, Da Costa et al. (1991) derive masses for the Galaxy between 4.5 and $9 \times 10^{11} M_\odot$. In the following, the calculations are performed for an effective $M_G = 5 \times 10^{11} M_\odot$. An increase in

the Galactic mass by a factor of 2 would increase the estimated perigalactic distances by a factor of 1.2. Since the tidal force seen by the satellite depends on how deeply it penetrates the potential well of the Galaxy a factor of uncertainty of 2 in the effective Galactic mass is not unreasonable. A mean orbital eccentricity of 0.5 is assumed but the results are not very sensitive to this assumption.

The total masses of the dSphs derived using the Illingworth method (Section 7.1.1) and the tidal radii given in Table 4 were used to compute the expected perigalactic distances shown in Table 11. With the exception of Leo I and Sextans, the other six dSphs have relatively well defined estimates of their perigalactic distances (subject to the assumptions inherent in the method). Draco, Ursa Minor, Carina and Leo II all have predicted perigalactic distances of less than 30 kpc which suggests, given their current distances and galactic velocities, that they are all on fairly elliptical orbits ($e > 0.5$).

A comparison of expected perigalactic distance with current galactocentric distance is shown in Fig. 4. It is clear from this diagram that both Sextans and Sculptor are candidates for systems undergoing tidal disruption (see Section 5). Furthermore, both of these systems have positive galactocentric radial velocities $\sim 70 \text{ km s}^{-1}$ and so presumably their true perigalactic distances are much smaller than their current distances and therefore within the tidal disruption regime. Of course, if their dynamical mass is an overestimate of their true mass, then this conclusion holds even more strongly.

Our values of D_{pg} agree with those estimated by Hodge & Michie (1969; hereby HM69) within the errors, for Sculptor, Fornax, Leo I and Leo II. However, both Draco and Ursa Minor have much smaller perigalactic distances than those estimated in this earlier paper; this difference is mostly due to the low masses assumed for these galaxies by Hodge &

Table 11. The expected perigalactic distances.

Galaxy	D_{pg} (kpc)	$ T/V $
Carina	29 ± 8	0.015 ± 0.012
Draco	17 ± 4	0.005 ± 0.002
Fornax	54 ± 8	0.037 ± 0.018
Leo I	53 ± 31	0.01 ± 0.02
Leo II	24 ± 7	0.001 ± 0.001
Sculptor	65 ± 11	0.3 ± 0.15
Sextans	106 ± 37	0.8 ± 0.8
Ursa Minor	28 ± 5	0.02 ± 0.01

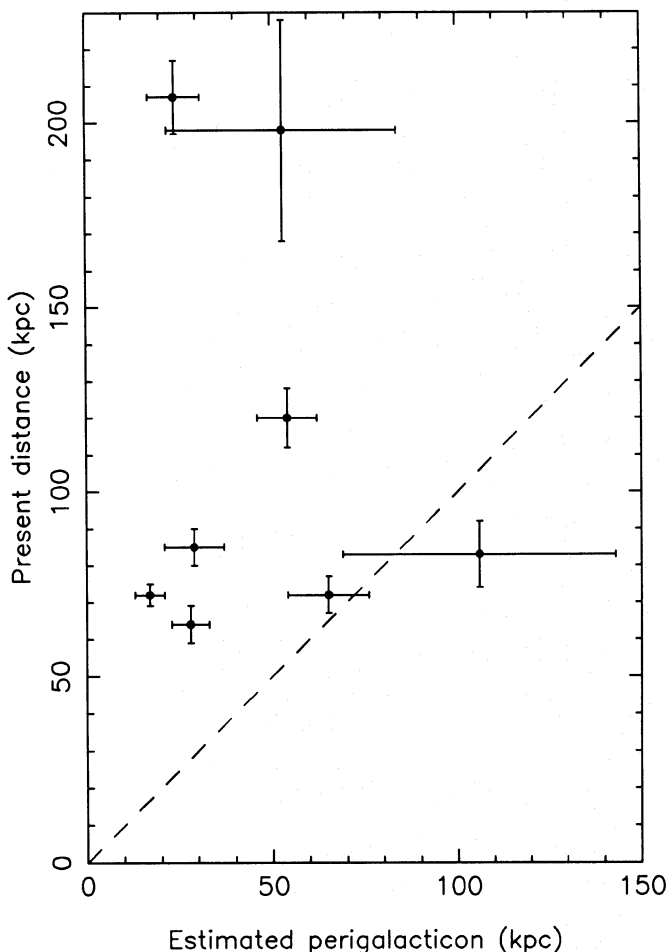


Figure 4. The perigalactic distances estimated from the model-fit tidal radius compared to the present day distances of the dSphs. If the true perigalactic distance of a satellite system (which will always be less than or equal to the current distance) moves a point to the right of the dashed line then the satellite should have experienced significant tidal impulses in the past and may be in the process of irreversible disruption. Both Sextans and Sculptor, with current galactocentric radial velocities of $\sim +70 \text{ km s}^{-1}$, must have true perigalactic distances significantly less than or equal to their present day distance and hence probably lie well within the disruption regime.

Michie. Their values were derived from the total luminosities, assuming a solar mass-to-light ratio.

7.3 The effect of the tidal force

Following HM69, we calculate (Table 11) the effect of the tidal field of the Galaxy on the internal structure of the dSphs by evaluating the ratio of the tidal force relative to internal gravity

$$|T/V| \approx 2(1 - \epsilon^2)^{1/2} \frac{M_G r_t^3}{MD^3}, \quad (5)$$

with ϵ the ellipticity of the dSph, M_G the mass of the galaxy, M the mass of the dSph, r_t its tidal radius and D its distance from the Galaxy. Following HM69, we plot T/V as a function

of the concentration parameter and ellipticity (Figs 5a and b respectively). In both Figs 5(a) and (b), it is evident that there is some correlation between the strength of the tidal force (relative to internal gravity) and morphological parameters. The correlation is similar to the one found by HM69; interestingly Leo I and II seem to fit into the general trend, contrary to the conclusions of HM69, while Ursa Minor – owing to the much larger mass assigned to it here – appears to have too high an ellipticity for the calculated tidal force to fit the general trend. This is perhaps not too surprising given the apparent substructure in Ursa Minor along the major axis.

The concentration parameter can be modified by the effect of tidal forces on the outer structure of the dSph, since a large value of $[T/V]$ should accompany a larger extent of the outer parts (relative to the core size). Fig. 5(a) qualitatively confirms this prediction. The fact that ellipticity also follows the trend suggests at least qualitatively that the morphology of the dSphs is influenced strongly by the tidal interaction with the Galaxy; in which case we would expect to find that the majority of the dSphs have a projected direction of orbital motion along their major axis. The preliminary measures of the proper motions of Draco and Ursa Minor by Scholz & Irwin (1994) and of Sculptor by Schweitzer & Cudworth (1995) support this conjecture.

7.4 Extra-tidal stars?

As can be seen in Fig. 2, in all eight dSphs the one-component King models cease to fit the data beyond the ‘calculated’ tidal radius. This excess of stars – which we will refer to as ‘extra-tidal stars’, for convenience – extends out to distances of more than twice the ‘tidal radius’ in many cases, and can account for up to 30 per cent of the integrated light from the dSph.

The effect is significant at least at the 5σ level. The evaluation of the contribution of foreground stars (and background galaxies) to the measured number densities is clearly crucial for the determination of the shape of the radial profile in these outer regions. As mentioned in Section 2.4, we have made full use of the unvignetted parts of each plate, either directly, by simply averaging the number density of images over the whole region processed, or indirectly, by examining the asymptotic radial fall-off of suitably binned number-density counts. In order for the ‘extra-tidal’ points to disappear the background levels would have to be in error by $\sim 5\sigma$ and would end up lying above most of the points in the outer regions of the radial plots.

Adoption of two-component models that can accommodate the possibly different densities and spatial distributions of dark and luminous matter, even with different amounts of anisotropy in the velocity distribution, still fail to account for this apparent overdensity in the outer regions (without significantly worsening the fit in the inner regions), as can be seen in the case of Carina (see Mateo et al. 1993, their figs 6 and 7).

The possibility of the existence of ‘extra-tidal’ stars, in the above sense, has been suggested in the past. Van Agt (1978) was the first to suggest the presence of ‘extra-tidal’ stars in Sculptor, based on his survey of variable stars in this galaxy. Although his estimate of the tidal radius of Sculptor is about 20 arcmin lower than our own estimate, there is still a signifi-

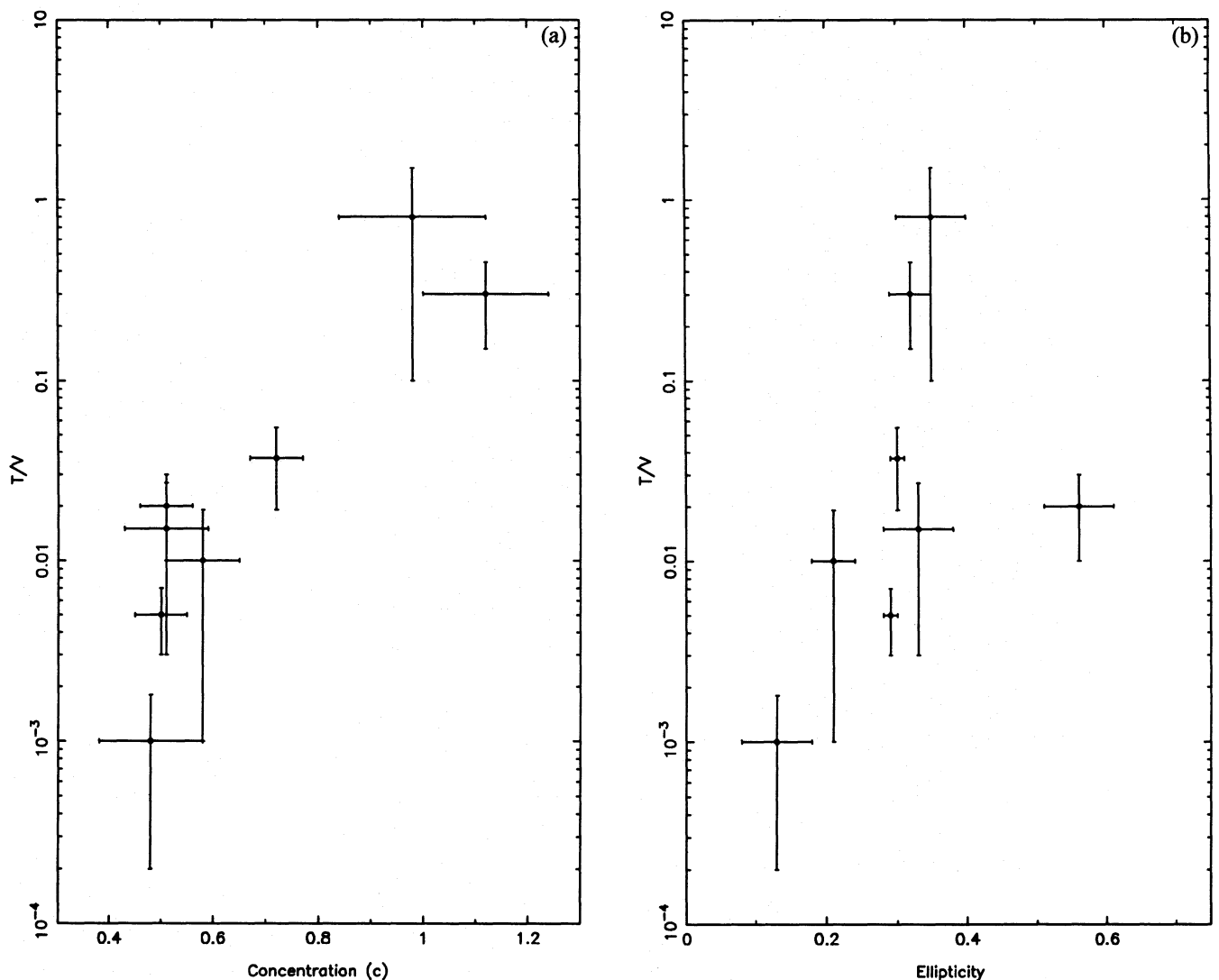


Figure 5. The ratio of the tidal force to internal gravity of the dSphs appears to be well correlated with (a) the concentration parameter and (b) the ellipticity of the dSphs. This suggests that Galactic tidal forces play a considerable role in determining the morphological appearance of the dSphs.

cant number of variables beyond our tidal radius, lying in a bipolar distribution. Eskridge (1988a,c) noted a similar effect in his profiles of Sculptor and Fornax as we did. Gould et al. (1992) claimed to have found possible Sextans members several kpc away from Sextans. However, this is the first time it has clearly been seen in so many of the dSphs and adds further support to the conjecture that the morphology of most Galactic dSphs is strongly influenced by the external Galactic tidal field.

Different interpretations are possible for these ‘extra-tidal’ stars (if they prove indeed to be members of the dSphs). Innanen & Papp (1979) interpreted the extra-tidal stars, observed by Van Agt (1978) in Sculptor, as being stars along the Galactic orbit plane; such stars – when in low-eccentricity orbits – can most effectively survive pruning by the galactic tide. Seitzer (1985) suggests that these ‘extra-tidal’ stars are indicative of ongoing tidal stripping, or of systems that have still not attained dynamical equilibrium. Oh, Lin & Aarseth

(1995) predict the presence of such tidal streams, from n -body simulations of dSphs undergoing significant tidal interaction with the host galaxy. It is noteworthy that simulations of dSphs in the tidal field of the Galaxy by Piatek & Pryor (1994) rendered density profiles qualitatively very similar to the ones we observed (Fig. 2), with the inner part of the density profile matching a King model, while there is a departure from that model at larger radii (their fig. 3). This departure is considered to be a signature of tides.

Taken together with the correlation of general morphological appearance and tidal effects, this suggests that external tidal forces play a far more significant role than previously realized, in determining the dynamical status and structure of the dwarf spheroidals, probably influencing our interpretation of the velocity dispersion of dSphs and its trend with dSph radius (cf. Kuhn & Miller 1989; Kuhn 1993). However, one should also keep in mind that the velocity dispersion may not be affected as significantly as one

might have thought: Oh, Lin & Aarseth (1994) predict that the velocity dispersion of the unbound but not yet dispersed stars is comparable to that in virial equilibrium just prior to the tidal disruption, thus probably not affecting the dark-matter estimates. Also, Piatek & Pryor (1994) note that the core region is least affected by tides. Thus the apparent M/L should vary with the position in the dSph, being lowest in the central regions. It will be important to test this prediction observationally.

From the results we have presented it is quite possible that at least some of the Galactic dSphs may not be internally bound at all; and that the majority do not seem to be in dynamical equilibrium in their outer parts. The currently observed population of dSphs might then represent the remnants of an originally much larger dSph population (e.g. Searle & Zinn 1978). Examples of possible relict populations are the 'moving groups' of stars found by Coté et al. (1993), Doinidis & Beers (1989) and Majewski (1992), whilst the Sagittarius dSph recently found by Ibata, Gilmore & Irwin (1994) is an excellent candidate for a dSph in the process of tidal disruption.

ACKNOWLEDGMENTS

We thank the UKSTU and Palomar telescope for making the photographic material available to us. DH was an AAO/SERC fellow during this work. We also wish to thank Gary Da Costa and M. Mateo for useful discussions and comments, and S. Demers for making available to us data before publication.

REFERENCES

- Binney J., Tremaine S., 1987, in *Galactic Dynamics*. Princeton, New Jersey
- Buonanno R., Corsi C. E., Fusi Pecci F., Hardy E., Zinn R., 1985, *A&A*, 152, 65
- Caldwell N., Armandroff T., Seitzer P., Da Costa G. S., 1992, *AJ*, 103, 840
- Carney B. W., Storm J., Jones R. V., 1992, *ApJ*, 386, 663
- Coté P., Welch D., Fischer P., Irwin M. J., 1993, *ApJ*, 406, L59
- Cudworth K. M., Olszewski E. W., Schommer R. A., 1986, *AJ*, 92, 766
- Da Costa G. S., Hatzidimitriou D., Irwin M. J., McMahon R. G., 1991, *MNRAS*, 249, 473
- Dekel A., Silk J., 1986, *ApJ*, 303, 39
- Demers S., Kunkel W. E., Krauter A., 1980, *AJ*, 85, 1587
- Demers S., Harris W. E., 1983, *AJ*, 88, 329
- Demers S., Beland S., Kunkel W. E., 1983, *PASP*, 95, 354
- Demers S., Irwin M. J., 1993, *MNRAS*, 261, 657
- Demers S., Irwin M. J., Gambu I., 1993, *MNRAS*, 266, 7
- Demers S., Irwin M. J., Kunkel W. E., 1994, *AJ*, 108, 1648
- Demers S., Battinelli P., Irwin M. J., Kunkel W. E., 1995, *MNRAS*, 274, 491
- Doinidis S. P., Beers T. C., 1989, *ApJ*, 340, L57
- Eskridge P. B., 1988a, *AJ*, 95, 1706
- Eskridge P. B., 1988b, *AJ*, 96, 1336
- Eskridge P. B., 1988c, *AJ*, 96, 1352
- Eskridge P. B., 1988d, *AJ*, 96, 1614
- Faber S. M., Lin D. N. C., 1983, *ApJ*, 266, L17
- Godwin P. J., 1985, in Goodman J., Hut P., eds, *Dynamics of Star Clusters*. Reidel, Dordrecht, p. 77
- Gould A., Guhathakurta R., Richstone D., Flynn C., 1992, *ApJ*, 388, 345
- Hargreaves J. C., Gilmore G., Irwin M. J., Carter D., 1994a, *MNRAS*, 269, 957
- Hargreaves J. C., Gilmore G., Irwin M. J., Carter D., 1994b, *MNRAS*, 271, 693
- Hodge P. W., 1961a, *AJ*, 66, 249
- Hodge P. W., 1961b, *AJ*, 66, 384
- Hodge P. W., 1962, *AJ*, 67, 125
- Hodge P. W., 1963, *AJ*, 68, 473
- Hodge P. W., 1964a, *AJ*, 69, 438
- Hodge P. W., 1964b, *AJ*, 69, 853
- Hodge P. W., 1966, *AJ*, 71, 204
- Hodge P. W., 1971, *ARA&A*, 9, 35
- Hodge P. W., 1982, *AJ*, 87, 1668
- Hodge P. W., Michie, 1969, *AJ*, 74, 587
- Hodge P. W., Smith D. W., 1974, *ApJ*, 188, 19
- Holmberg E., 1958, *Medd. Lunds Astron. Obs.*, No. 2, 136
- Ibata R. A., Gilmore G., Irwin M. J., 1994, *Nat*, 370, 194
- Illingworth G., 1976, *ApJ*, 204, 73
- Innanen K. A., Papp K. A., 1979, *AJ*, 84, 601
- Irwin M., Trimble V., 1984, *AJ*, 89, 83
- Irwin M. J., 1985, *MNRAS*, 214, 575
- Irwin M. J., Bunclark P. S., Bridgeland M. T., McMahon R. G., 1990, *MNRAS*, 244, 16P
- Kibblewhite E. J., Bridgeland M. T., Bunclark P. S., Irwin M. J., 1984, in Klinglesmith D., ed., *Proc. Astron. Microdensitometry Conf. NASA-2317*, NASA, Washington DC, p. 277
- King I. R., 1962, *AJ*, 67, 471
- King I. R., 1966, *AJ*, 71, 64
- Kormendy J., 1987, in Kormendy J., Knapp G. R., eds, *Proc. IAU Symp. 117, Structure and Dynamics of Elliptical Galaxies*. Reidel, Dordrecht, p. 139
- Kuhn J. R., Miller R. H., 1989, *ApJ*, 341, L41
- Kuhn J. R., 1993, *ApJ*, 409, L13
- Kunkel W. E., Demers S., 1977, *ApJ*, 214, 21
- Lake G., 1990, *MNRAS*, 244, 701
- Lynden-Bell D., Cannon R. D., Godwin P. J., 1983, *MNRAS*, 204, 87
- Majewski S. R., 1992, *ApJS*, 78, 87
- Mateo M., Olszewski E. W., Welch D. L., Fischer P., Kunkel W., 1991, *AJ*, 102, 914
- Mateo M., Olszewski E. W., Pryor C., Welch D. L., Fischer P., 1993, *AJ*, 105, 210
- Mighell M., 1990, *A&AS*, 82, 207
- Mould J., Aaronson M., 1983, *ApJ*, 273, 530
- Nemec J. M., Wehlau A., Mendes de Oliveira C., 1988, *AJ*, 96, 528
- Oh K. S., Lin D. N. C., Aarseth S. J., 1994, in Meylan G., ed., *Proc. ESO/OHP Workshop, Dwarf Galaxies*. p. 381
- Oh K. S., Lin D. N. C., Aarseth S. J., 1995, *ApJ*, 442, 142
- Olszewski E. W., Aaronson M., 1985, *AJ*, 90, 2221
- Paltoglou G., Freeman K. C., 1987, in de Zeeuw T., ed., *Proc. IAU Symp. 127, Structure and Dynamics of Elliptical Galaxies*. Reidel, Dordrecht, p. 447
- Piatek S., Pryor C., 1994, in Meylan G., ed., *Proc. ESO/OHP Workshop, Dwarf Galaxies*. p. 397
- Pryor C., Kormendy J., 1990, *AJ*, 100, 127
- Pryor C., 1992, in Longo G., Capaccioli M., Busarello G., eds, *Morphological and Physical Classification of Galaxies*. Kluwer, Dordrecht, p. 163
- Richstone D. O., Tremaine S., 1986, *AJ*, 92, 72
- Scholz R. D., Irwin M. J., 1994, in MacGillivray H. T., Thomson E. B., Lasker B. M., Reid I. N., Malin D. F., West R. M., Lorenz H., eds, *Proc. IAU Symp. 161, Astronomy from Wide Field Imaging*. Reidel, Dordrecht, p. 535
- Schweitzer A. E., Cudworth K. M., 1995, *BAAS*, 26, 1396
- Searle L., Zinn R., 1978, *ApJ*, 225, 357
- Seitzer P., 1985, in Goodman J., Hut P., eds, *Proc. IAU Symp. 113, Dynamics of Star Clusters*. Reidel, Dordrecht, p. 343
- Smecker-Hane T. A., Stetson P. B., Hesser J. E., 1994, *AJ*, 108, 507
- Stetson P. B., 1979, *AJ*, 84, 1149

1378 *M. Irwin and D. Hatzidimitriou*

- Suntzeff N. B., Aaronson M., Olszewski E. W., Cook K. H., 1986, AJ, 91, 1091
Suntzeff N. B., Mateo M., Terndrup D. M., Olszewski E. W., Geisler D., Weller W., 1993, ApJ, 418, 208
Tremaine S., Gunn J. E., 1979, Phys. Rev. Lett., 42, 407
UK Schmidt Telescope Unit, Handbook, 1983, Royal Observatory, Edinburgh
Van Agt S. L. Th., 1978, Publ. D. Dunlop Obs., 3, 205
de Vaucouleurs G., Ables H. D., 1968, ApJ, 151, 105
Vogt S. S., Mato M., Olszewski E. W., Keane M. J., 1995, AJ, 109, 151
Walker A. R., 1992, ApJ, 390, L81
Webbink R. F., 1985, in Goodman J., Hut P., eds, Proc. IAU Symp. 113, Dynamics of Star Clusters. Reidel, Dordrecht, p. 541
Zaritsky D., Olszewski E. W., Schommer R. A., Peterson R. C., Aaronson M., 1989, ApJ, 345, 759